POLITECNICO
MILANO 1863

SCUOLA DI INGEGNERIA INDUSTRIALE
E DELL'INFORMAZIONE

Potential modelling of tubercled wings

Tesi di Laurea Magistrale in
Ingegneria Aeronautica - Aeronautical Engineering

Author: **Sebastiano Vianello**

Student ID: 952633
Advisor: Giuseppe Quaranta
Co-advisors:
Academic Year: 2021-2022

Acknowledgements

Prima di iniziare l'elaborato conclusivo della mia carriera accademica vorrei ringraziare chi ha reso tutto possibile.
Ringrazio il Professor. Giuseppe Quaranta per la fantastica opportunità di tesi proposta, il supporto durante l'attività di sviluppo e i consigli sempre preziosi per raggiungere questo risultato.
Ringrazio tutti i miei compagni del Dynamis. Per tutti i millimetri di carbonio grattati, per tutte le notti in officina e i momenti fantastici spesi insieme.
Ringrazio tutti i miei amici di Pordenone, sempre presenti in ogni momento, bello e brutto, e pronti a sostenere il mio percorso. Ringrazio Jessica, per essere sempre stata al mio fianco, per avermi supportato (e sopportato) in tutti i momenti di difficoltà e per avermi spinto a fare meglio ogni volta che volevo mollare. Ti amo tanto.
Ringrazio Giulio, Carlotta e Costanza.
Non potrei essere più orgoglioso di avere voi come padre, madre e sorella. Grazie per tutto.
E ringrazio Beppino e Wilma.
Che forse, portandomi da bambino a vedere i treni in stazione, avevano capito prima di tutti la strada che avrei preso.

Abstract

The development of wavy leading edge wings originates from studying the hunting behaviour of the humpback whales, which exploits aggressive turning ratios to increase the chance of a successful hunt. Observing the animal it was deduced that the ventral flippers are the main contributors in achieving such tight curves. The study of such movement could produce useful application in the Urban Mobility Vehicles, where small, efficient rotors are required due to constraint in maximum dimensions and ever increasing needs of extended operative range. This geometry could be implemented in wind turbines design to expand the operative range, which leads to increased power generation and larger revenues. The flipper shape itself produces a reduction in induced drag, due to the planform design, but the main objects of interest are the leading edge tubercles on said flippers. These tubercles are main contributors in the generation of leading edge vortices, which exchanges momentum within the boundary layer and delays separation. The wavy leading edge produces a reduction in lift in small angle of attack operations, but contributes to increase the value of maximum angle of attack before separation occurs. A Doublet-Source-Lattice numerical code is developed to model the wings of interest, and it is coupled with a vortex line model to represent the counter rotating vortices inducing surface velocity. Different vortex core models are modelled and their positioning is evaluated to correctly represent the surface induced velocities. The reference wing is analyzed in pitching and plunging conditions to assess the loads on a dynamic system. The modelled vortices produces an increase in surface velocities, resulting in extended operative range.

Keywords:potential;tubercles;theodorsen;vortex line

Abstract in lingua italiana

Lo sviluppo delle ali con bordo d'attacco ondulato nasce dallo studio del comportamento di caccia delle megattere, che sfruttano ratei di virata aggressivi per aumentare le possibilità di successo della caccia. Osservando l'animale si è dedotto che le pinne ventrali sono le principali responsabili del raggiungimento di tali ratei di virata. Lo studio di questo movimento potrebbe produrre utili applicazioni nei veicoli per la mobilità urbana, dove sono richiesti rotori piccoli ed efficienti a causa dei vincoli di dimensioni massime e delle esigenze sempre più pressanti di autonomia operativa. Questa geometria potrebbe essere implementata nella progettazione di turbine eoliche per ampliare l'inviluppo operativo, con conseguente aumento della produzione di energia e dei ricavi. La forma della pinna in sé produce una riduzione della resistenza aerodinamica indotta, grazie al design della forma, ma gli oggetti principali di interesse sono i tubercoli del bordo d'attacco di tali pinne. Questi tubercoli sono i principali responsabili della generazione di vortici sul bordo d'attacco, che scambiano quantità di moto nello strato limite e ritardano la separazione. Il bordo d'attacco ondulato produce una riduzione della portanza nelle operazioni con piccoli angoli d'attacco, ma contribuisce ad aumentare il valore dell'angolo d'attacco massimo prima che avvenga la separazione. Per modellare le ali di interesse è stato sviluppato un codice numerico Doublet-Source-Lattice, accoppiato a un modello di linea vorticosa per rappresentare i vortici controrotanti che inducono la velocità superficiale. Vengono modellati diversi modelli di nucleo di vortici e viene valutato il loro posizionamento per rappresentare correttamente le velocità indotte dalla superficie. L'ala di riferimento viene analizzata in condizioni di beccheggio e di picchiata per valutare i carichi su un sistema dinamico. I vortici modellati producono un aumento delle velocità di superficie, con conseguente estensione della regione di operatività.

Parole chiave:potenziale;tubercoli;theodorsen;linea vorticosa

Contents

1 | Introduction

1.1. Biomimicry: from evolution to engineering solutions

Millions of years of evolution provides an excellent source of inspiration for engineering problems.
The nose of the Shinkansen, the first high-speed train developed in Japan in the 1960, was inspired by the kingfisher, which has evolved in such a way to reduce impact drag when fishing. Shark skin is used as a mock design to engineer low resistance surfaces, creating artificial denticles whose purpose is to reduce skin drag. Such technology has found applications in the design of low drag swimsuits ([27]) or coating of wind turbines blades ([9]).
Airbus is developing scale model of future aircrafts with wing tips design directly inspired by long cruising birds, to reduce vortex drag, increase the aircraft efficiency and improve aeroelastic performance of the wing. Wavy leading edge wings are another of example of such methodology. Due to the increasing interest towards urban mobility, using multirotor vehicles, with the introduction of electric propulsion, strict requirements in noise reduction, and limited dimensions allowances, the demanding for wings and rotors with high lifting capabilities is steadily increasing. Being the wing lift defined as:

$$L(h, \alpha, S, V) = \frac{1}{2}\rho(h) S C_L(\alpha) V^2 \tag{1.1}$$

where h is the altitude, S is the wing surface, α is the wing angle of attack and V is the wing velocity. The velocity can be decomposed in two components:

$$V(r) = V_\infty + \omega r \tag{1.2}$$

where V_∞ is the wing traslational velocity, ω is the rotor rotational speed and r is the distance of the evaluated section from the rotor hub. To achieve a certain amount of lift, at fixed altitude and in hover conditions (which provides the assumption of $V_\infty = 0$, the parameters that can be modified are then S, α and ω.
A surface increase produces an increase in the wingspan, which could lead to near trans-sonic flow regime at the wing tip, thus generating a considerable increase in drag and sound emis-

sions. A weight increase has to be taken into account as well, which would be detrimental for the vehicle overall efficiency, thus range and operational cost.
On the other hand, the increase in rotor rotational speed replicates the trans-sonic problem aforementioned, while increasing the power requirement by each rotor, with effects on the overall endurance and range of the rotorcraft. This could lead to reduced lifespan of the components as well, being the higher rotational speed a source of higher stresses on the rotor components.
The final parameter that can be modified is the wing lift, by changing the $C_L(\alpha)$. This can be done by changing two parameters: C_{L_α}, which is typical of each airfoil section, or α, achievable by increasing the blade pitch. However, as shown in Figure 1.1, the ideal lift coefficient, represented by the straight line marked with "Eq. (4.57)", departs from the real lift coefficient curve, represented by the markers, due to separation occurring.

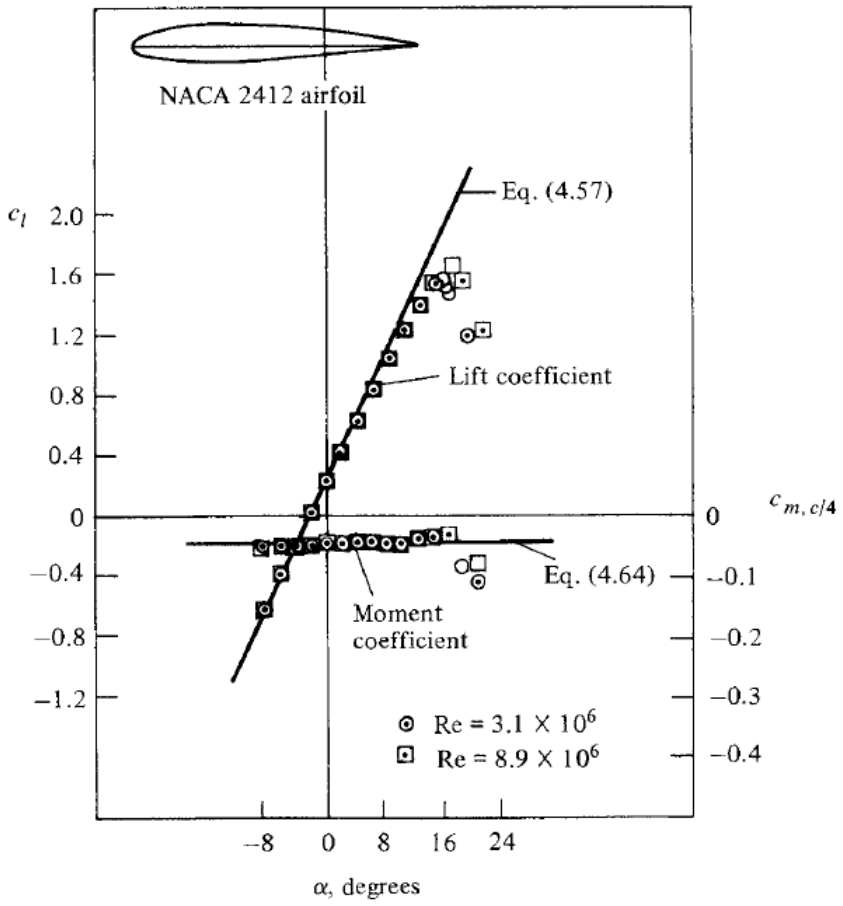

Figure 1.1: NACA 2412: ideal vs viscous polar (from [17], page 322)

The separation from wing profile occurs when the adverse pressure gradient produces a null

wall shear stress when evaluated at the wall:

$$\tau_w = \mu \frac{\partial u}{\partial y}\bigg|_{y=0} \tag{1.3}$$

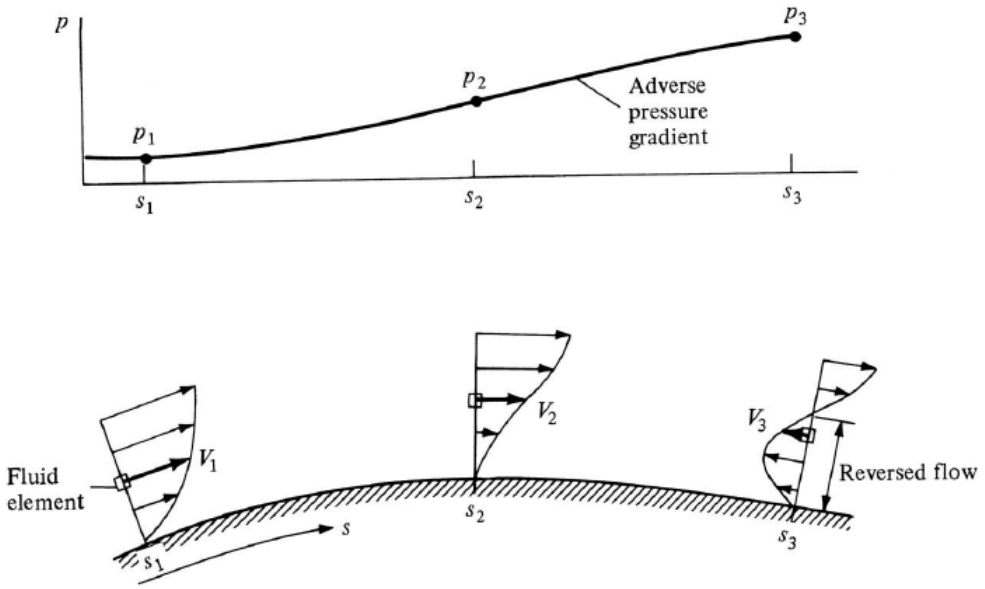

Figure 1.2: Graphical representation of adverse pressure gradient (from [17], page 897)

This phenomena prevents the wing from being able to work at high angle of attack, reducing the lift generation capabilities of the wing. To achieve higher lift at a given angle of attack, the so-called 'High Lift Devices' two can be exploited. Those devices are placed usually either on the leading edge or on the trailing edge of the wing profile. While the trailing edge flaps produces an increase in the maximum achievable lift, leading edge slats ensures a wider range of operability for the wing, delaying the flow separation at higher angles of incidence. However, due to the requirements of dedicated kinematics and actuators, their usage in rotorcrafts applications is not feasible.

On a rotorcraft, the rotorblades might experience some degree of local stall, due to low amplitude oscillations occurring on the rotorblade. The actuation of leading edge flaps to delay said stall is a task close to impossible to achieve, due to the frequency and potential unpredictability of the phenomena. To cancel or smoothen the stall characteristics of the blade, increasing the wing section C_L at higher angles of incidence, a passive flow controller is required. For this scope, the usage of leading edge tubercles is introduced.

Wavy leading edge wings are inspired from the ventral fin of the humpback whale. Such whale, despite not being the biggest cetacean in the ocean ([8]), is the one with bigger ventral fins

compared to the overall body dimension, with an average fin length sparring from 25% to 33% of the overall body length. The fin recalls the shape of a wing of aspect ratio of $3.6 - 7.7$, and along the leading edge a distribution of tubercles can be found.

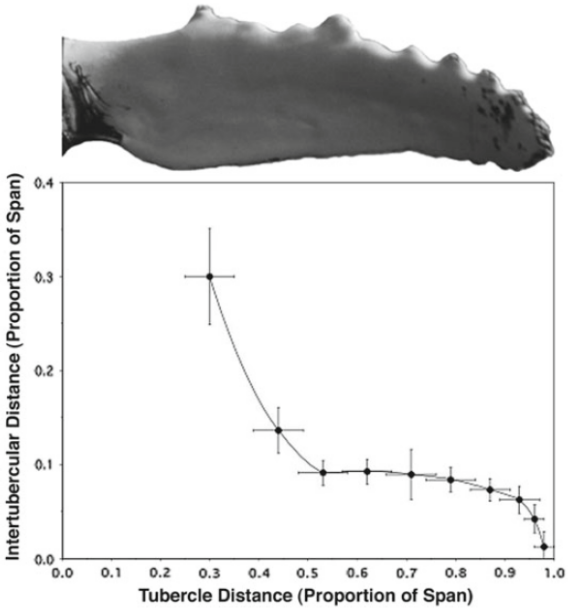

Figure 1.3: Tubercles distribution on humpback whale fin (from [8], page 8)

Such tubercles evolved through time to support the hunting pattern of the humpback whale. Unlike other species in the same family, which rely on hunting in a straight line, humpback whales hunt by executing tight turns, which ensures the capability of enlarging the number of possible preys. As shown in figure 1.4, the turning radius can change drastically depending on the bank angle of the mammal. The turn diameter is defined as a function of the centrifugal force, the whale mass and velocity:

$$R(m, V, F_c) = \frac{mV^2}{F_c} \tag{1.4}$$

where the centrifugal force is equal to the lift generated by the ventral fins:

$$L(\alpha, \phi, V) = \frac{1}{2}\rho S\, C_L(\alpha) \sin\phi V^2 \tag{1.5}$$

where α is the fin angle of attack, ϕ is the bank angle of the whale, V is the whale velocity. Equalling equations 1.4 and 1.5 the relation between turning radius an aerodynamic properties of the wing is found:

$$R(m, \alpha, \phi) = \frac{4m}{\rho S\, C_L(\alpha) \sin\phi} \tag{1.6}$$

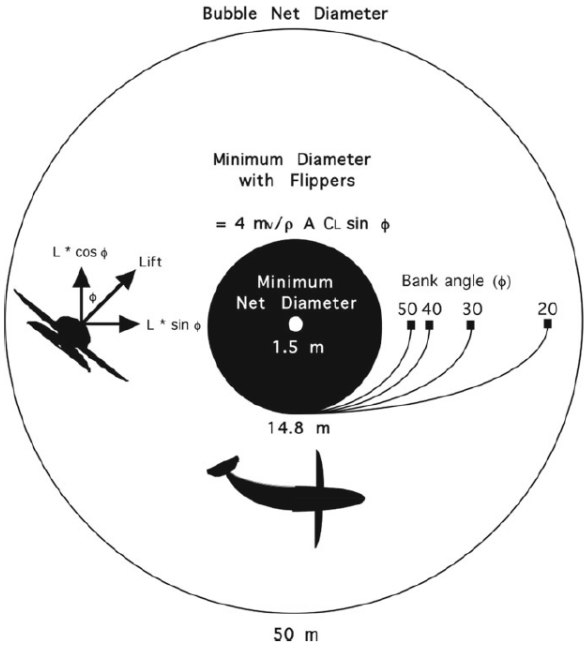

Figure 1.4: Humpback whale hunting patterns (from [8], page 10)

The relation between the fin $C_L(\alpha)$ and the radius shows that a reduction of turning radius is achievable by increasing the $C_L(\alpha)$ of the fin. It is quite clear that an extreme increment of α would lead to a drastic reduction of the turning radius, but as described above the excessive increment in the angle of attack will lead to flow separation on the suction side of the wing. [4] where the first to propose the tubercles as a mean of flow control on the flippers, by proposing the tubercles as a mean of reduction of the induced drag. The other effect of wavy leading edge, which is the one considered in this study, is the delay of stall when high values of A.o.A are reached.

1.2. Stall behaviour

The effect of tubercles on stall delay were thoroughly studied for implementation in stall delay applications. The studies were conducted through a large plethora of methods: experimental flow visualization ([20], [18]), high fidelity numerical simulations (Euler ([19]), RANS [7], LES [26]) and medium-fidelity numerical simulations ([23]). A large plethora of Reynolds numbers was analyzed as well sparring from really low Reynolds of 800 ([10]) up to high Reynolds of $5.5 \cdot 10^5$ ([20]). According to [18] a linear increment in lift coefficient for both straight and wavy leading edge wings was determined up to $\alpha = 7\,\text{deg}$, albeit with different slopes ($\frac{dC_L}{d\alpha} = 4.87$ and 4.58 respectively). The former wing reaches a maximum lift coefficient of 0.7. Reaching $\alpha = 8\,\text{deg}$, the straight wing stalls, with stall recovery happening at $\alpha = 13\,\text{deg}$, when the overall lift begins to rise again. On the other hand the wavy wing lift coefficient rises up to $C_L = 0.86$ at $\alpha = 11\,\text{deg}$. When this value is reached, the lift coefficient remains constant up to $\alpha = 15\,\text{deg}$, when the flow detaches from the wing and the C_L decreases rapidly. Further increasing the angle of attack the lift coefficient of the two wings approaches the same value.

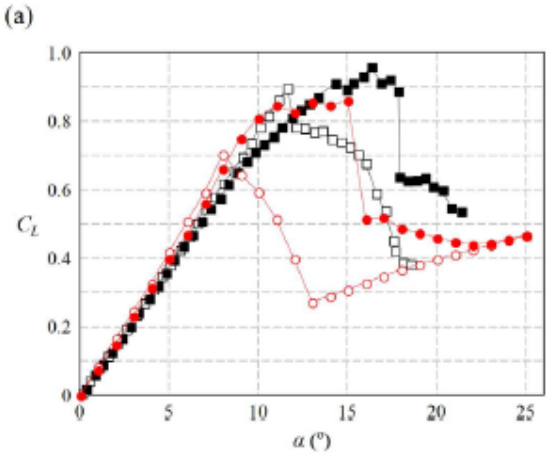

Figure 1.5: C_{L_α} comparison. Hollow circles and squares represent the base geometry. Full circles and squares represent the wavy geometry. [18]

According to [18] the vortices generated by the tubercles plays a fundamental role in the stall delay. As shown in picture b) of Figure 1.6 two counter rotating structures are responsible for the momentum exchange within the boundary layer.

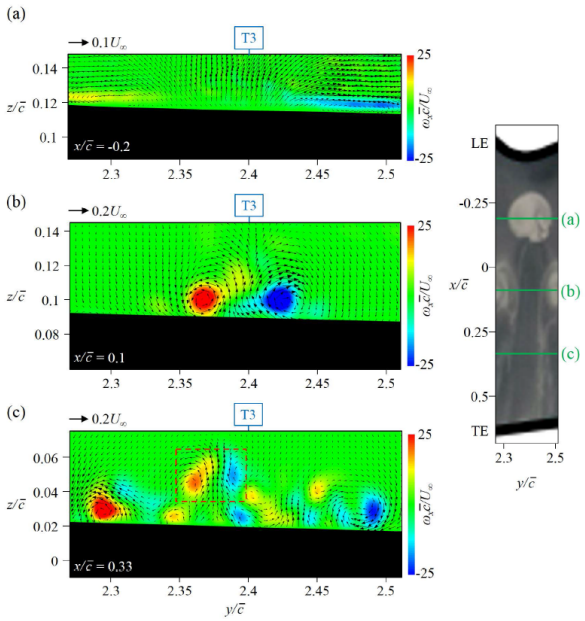

Figure 1.6: Velocity profiles at various wing sections ([18])

This phenomena leads to varying C_p distribution along the wing span. In the through sections, a lower $-C_p$ value is observed, while in the peak sections a higher $-C_p$ value is observed, as shown in Figure 1.7, where the minimum $-C_p$ value is achieved in through sections (denoted with T), while on the wing peaks bigger values of $-C_p$ are achieved, with the peak achieved closer to the leading edge.

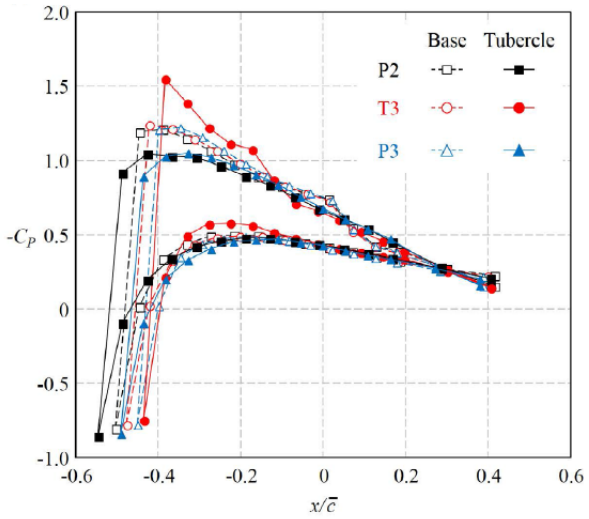

Figure 1.7: $-C_p$ chord distribution at different span sections ([18])

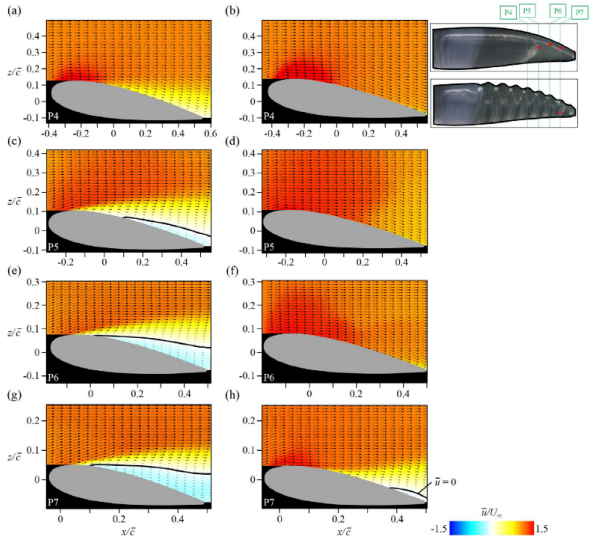

Figure 1.8: Velocity profile along wing chord, $\alpha = 9°$ [18]

At low α, this does not compensate the planar form, producing the results shown in 1.5. As seen in 1.8 the presence of the vortices on the wing back introduces a component of momentum exchange within the boundary layer, which delays the stall insurgence. Hrynuk *et al.* ([15]) proposed a study on the effect of dynamic stall, pitching a baseline and a modified NACA-0012 wing from 0° to 50° and observing the formation of DSV (Dynamic Stall Vortex). They demonstrated the role of the tubercles in achieving consistent dynamic lift, and their role in the delay of stall occurrence, thus increasing the operating range of the wing. Bing Feng Ng *et al.* ([21]) performed an analysis of a wing undergoing a pitching motion of $\pm = 10°$ at reduced frequencies $k = 0.1$ and $k = 0.4$. The tubercle presence reduces the quasi-steady lift coefficient by 2% due to L.E. suction reduction. It should be noted that such analysis is carried using an unmodified UVLM (UnsteadyVortexLatticeMethod), which does not take into account the effect of the counter rotating vortex. The reduction of the leading edge suction was observed by Rostamzadeh *et al.* ([25]), due to spanwise flow movement, which is favoured by the geometrical configuration of the wing, with the flow moving from the wing through to the wing peak. This sounds counter-intuitive, but it's driven by the pressure reduction which occurs on the section peak, having a longer chord.

1.3. Rotorcraft Applications

As pointed at the beginning of this chapter, a particular field which interests the tubercles applications is the urban mobility one. Garrow *et al.* ([11]) evidenced a slow, but ever increasing, introduction of UAM vehicles, especially in densely inhabited areas. Various possibilities were considered, from vectored thrust configurations to multicopters and rotorcrafts. All these configurations used rotors with different section geometry, propeller diameters and number of blades. Maestre *et al.* ([2]) thoroughly examined different propeller number and diameters to determine the ideal configuration for a tandem wing eVTOL aircraft. A reduction in diameter provides lower noise emission, higher ground clearance and an higher degree of redundancy to increase the safety in OEI conditions. Bigger propellers would, on the other hand, reduce disk loading and power requirements. Butt *et al.* ([5]) tested through CFD analysis, using RANS turbulence models, two, three and four blades geometries, with both clean leading edge and tubercled leading edge. For each geometry an increase in the propeller efficiency η_p is observed, with the increase in efficiency from the baseline solution becoming larger at higher advance ratios J. This was correlated with a reduction in spanwise flow, stall delay and reduction of wingtip vortices. Colpitts *et al.* ([6]) analyzed the effect of tubercles introduction and its shape compared to a baseline rotor blade. Different tubercles geometry are tested in comparison to the baseline geometry. An improvement of 9.5% in rotor Figure Of Merit is observed. Smaller and denser distribution of tubercles produces similar distribution of pressure of the wing compared to the baseline geometry, while having mayor benefit in drag reduction. Tubercles with *sin* shape performs better in improving FOM, reducing rotor C_P (Coefficient of Power) while increasing its C_T (Coefficient of Thrust). Tubercles following a power law improves the rotor C_T while increasing at well the C_P due to increased skin friction.

1.4. Thesis motivation

The scope of this work will be the evaluation of a modified potential method to better estimate the effect of the aforementioned vortex structures. The dependency of the studies geometry on viscous phenomenas should discourage from usage of panel methods, due to the inviscid nature of such numerical solution. CFD solutions are better suited for this work, being more capable of capturing the complexity of these flow structures. Panel methods, however, are far more used and suited for the initial design and evaluation of a wing geometry, due to their implementation easiness and fast computational times. The motivation of this work is to modify a classical virtual singularities panel method to predict the influence of leading edge tubercles not only from a geometrical point of view, but from a viscous one as well. The advantage of a potential method compared to F.V. (Finite Volume) methods can be summed up in:

- Reduced programming effort
- Reduced computational cost
- Accurate flow description for applications at high Reynolds numbers
- Good prediction of viscous flows with minor tweaks

On the other hand, the neglected viscosity components in formulating the potential problem leads to a loss in insight in more complex flow structures, such as eddies formation and vortex shedding. The main effort will be in trying to emulate the vortex shedding typical of the considered geometries, by implementing a vortex line originating in prescribed locations and evaluating its effect in steady and unsteady conditions. This work will be structured in 5 different chapters, which are summarized as follows:

1. Chapter 1 - Introduction: a description of the inspiration of this work is given
2. Chapter 2 - Physical and Numerical Modelling: the physical and numerical frameworks are given. A description of the vortex model chosen and of the free vortex methodology implemented is given.
3. Chapter 3 - Validation of numerical solver: the designed solver is validated through comparison with known solutions.
4. Chapter 4 - Tubercles assessment: the effect of leading edge tubercles is assessed, both via steady state and unsteady solutions. The analysis of a pitching and plunging wing is given.
5. Chapter 5 - Conclusions: the final conclusions are made. The results are further discussed and possible future development are assessed.

2 | Physical and Numerical Modelling

In the following section the physical modelling of the proposed problem is discussed. A description and derivation of the fundamental fluid dynamics equations will be proposed, with the derivation of the Navier-Stokes equations. The linearization of the fundamental equations will be proposed to obtain the Laplace equation and its numerical implementation. The implementation of the free vortex will be discussed and the relaxation of the numerical singularity. Subsequently, the mechanical continuum of beams and plates will be discussed, with the derivation of the fundamental equations, beam kinematics description and FEM methodology implementation.

2.1. Navier-Stokes Equations

Navier-Stokes equations are the fundamental equations to describe the dynamic of the fluid. The whole description can be discretized with 3 different equations: continuity equation, momentum equation and energy equation. Each equation is derived by considering a control volume and balance volume's I/O. All the described equations are taken from the book *Fundamentals of aerodynamics* by John D. Anderson ([17]).

2.1.1. Continuity equation

The mass balance across the control volume is:

$$\dot{m} = \rho V_n A \tag{2.1}$$

where ρ is the fluid density, V_n is the velocity component normal to the control volume surface and A is the control volume surface. Applying the mass conservation, and considering the output surface of the control volume, a balance between the mass within the control volume and the aforementioned surface can be defined, and by applying the divergence theorem to the flux through the control surface 2.2 can be achhieved.

$$\iiint_V \frac{\partial}{\partial t}\rho d\mathcal{V} + \iint_S \rho \mathbf{v} \cdot \mathbf{dS} = \iiint_V \frac{\partial}{\partial t}\rho d\mathcal{V} + \nabla \cdot (\rho \mathbf{v}) d\mathcal{V} = 0 \tag{2.2}$$

Hence the mass conservation equation can finally be rewritten as:

$$\frac{\partial \rho}{\partial t} + \boldsymbol{\nabla} \cdot (\rho \boldsymbol{v}) = 0 \tag{2.3}$$

2.1.2. Momentum equation

The force acting on a system can be written from Newton second law:

$$\mathbf{F} = m\mathbf{a} = m\frac{d}{dt}m\mathbf{V} \tag{2.4}$$

The force term can be decomposed in 3 different terms:

$$\iiint_{\mathcal{V}} \rho \mathbf{f} d\mathcal{V} \quad \text{is the body force} \tag{2.5a}$$

$$-\iint_{\mathcal{S}} p\mathbf{dS} \quad \text{is the pressure force} \tag{2.5b}$$

$$\mathbf{F}_{visc} \quad \text{are the viscous forces} \tag{2.5c}$$

Rearranging equation 2.5 and applying the divergence theorem the momentum equation is obtained:

$$\iiint_{\mathcal{V}} \frac{\partial}{\partial t}(\rho \boldsymbol{v}) + \boldsymbol{\nabla} \cdot (\rho \boldsymbol{v})\boldsymbol{v} d\mathcal{V} = \iiint_{\mathcal{V}} -\nabla p d\mathcal{V} + \rho \mathbf{f} + \boldsymbol{F}_{viscous} d\mathcal{V} \tag{2.6}$$

The viscous term will be analyzed and decomposed when dealing with the equations linearization.

2.1.3. Energy equation

The balance of internal energy is defined as:

$$\delta q + \delta w = de \tag{2.7}$$

where δq is defined as the heat added to the system (positive when entering the system) δw is the external work done on the system (positive when leaving the system) and de is the system internal energy. It's necessary to define the values in function of their fluctuations through time and the control volume defined at the beginning of the chapter.

$$\iiint_{\mathcal{V}} \dot{q}\rho d\mathcal{V} \quad \text{is the volumetric rate of heat exchange} \tag{2.8a}$$

$$\dot{Q}_{visc} \quad \text{is the heat exchange due to viscous forces} \tag{2.8b}$$

$$\iiint_{\mathcal{V}} (\rho \boldsymbol{f} \cdot \boldsymbol{V}) d\mathcal{V} \quad \text{is the work due to body forces} \tag{2.8c}$$

$$-\iint_{\mathcal{S}} p\boldsymbol{V} \cdot \boldsymbol{dS} \quad \text{is the work due to pressure forces} \tag{2.8d}$$

$$\dot{\mathcal{W}}_{visc} \quad \text{is the work due to viscous forces} \tag{2.8e}$$

The rate of change in the control volume is defined, as the prior equations, for the internal volume and the outer surface of the control volume. The energy per unit mass is decomposed in two terms: the internal energy e and the kinetic energy $\frac{v^2}{2}$. The equations can be combined to

obtain the energy equation, and by applying the divergence theorem:

$$\iiint_{\mathcal{V}} \frac{\partial}{\partial t}\rho(e+\frac{v^2}{2}) + \nabla \cdot \rho(e+\frac{v^2}{2})\boldsymbol{V}\, d\mathcal{V} = \iiint_{\mathcal{V}} -\nabla p\boldsymbol{V} + \rho\dot{q} + \rho(\boldsymbol{f}\cdot\boldsymbol{V})d\sqsubseteq + \dot{\mathcal{Q}}_{visc} + \dot{\mathcal{W}}_{visc} \tag{2.9}$$

2.1.4. Inviscid flow hypotesis and linearization

Having defined the fundamental equations, to proceed to the linearization some hypotesis has to be imposed. These hypotesis spars directly from the 1^{st} Helmholtz theorem. Recalling equation 2.6, the viscous term can be neglected if the following considerations are made:

- $\vec{\nabla} \cdot \vec{u}, \rho$ are constant.
- Irrotational flow outside the boundary layer.
- Vorticity confined within the boundary layer.
- Bodundary layer and wake form a thin layer. This leads to a neglectable viscosity.
- The body forces contribution is either defined with a potential function or can be neglected.

From equation 2.3 and applying the incompressibility and irrotationality of the fluid the following equations can be defined:

$$\vec{\nabla} \cdot \vec{u} = 0 \tag{2.10a}$$

$$\vec{\nabla} \wedge \vec{u} = 0 \tag{2.10b}$$

$$\vec{u} \cdot \vec{n}\big|_{\partial\Omega} = b \tag{2.10c}$$

which represent, respectively, the incompressibility, irrotationality of the fluid and the non penetration boundary condition on the body surface. The first two terms can be developed as:

$$\vec{\nabla} \cdot \vec{u} = \frac{\partial u}{\partial x} + \frac{\partial v}{\partial y} + \frac{\partial w}{\partial z} = 0 \tag{2.11a}$$

$$\vec{\nabla} \wedge \vec{u} = \begin{vmatrix} \hat{x} & \hat{y} & \hat{z} \\ \frac{\partial}{\partial x} & \frac{\partial}{\partial y} & \frac{\partial}{\partial z} \\ u & v & w \end{vmatrix} = 0 \tag{2.11b}$$

With further derivation of the two equations, the velocity can be expressed in function of the Laplace equation:

$$\nabla^2 \vec{u} = \frac{\partial^2 u}{\partial x^2} + \frac{\partial^2 v}{\partial y^2} + \frac{\partial^2 w}{\partial z^2} = 0 \tag{2.12}$$

Recalling equation 2.10b and the vorticity confined to a thin region of the flow field, from the mathematical point of view a simply connected domain can be defined. This leads to the possibility of defining the velocity as function of a kinetic potential.

$$\vec{u} = \vec{\nabla}\Phi \tag{2.13}$$

then equation 2.10 can be rewritten as:

$$\vec{\nabla} \cdot \vec{u} = \vec{\nabla} \cdot \vec{\nabla}\Phi = \nabla^2\Phi = 0 \tag{2.14a}$$

$$\vec{\nabla} \wedge \vec{u} = \vec{\nabla} \wedge \vec{\nabla}\Phi = 0 \tag{2.14b}$$

$$\vec{u} \cdot \vec{n} = \vec{\nabla}\Phi \cdot \hat{n} = \frac{\partial \Phi}{\partial n} = b \tag{2.14c}$$

The fluid velocity is now defined as function of the Laplace operator, and the Laplace equation is respected. This equation is a second-order linear partial differential equation. The linearity gives the opportunity to sum and combine simpler flow equations to achieve a more complex flow field. Having defined the potential function and it's relation with the basic equations, the numerical implementation of said equations can be formulated, following the formulation proposed by Morino.

2.2. Numerical Implementations

2.2.1. Green function method

The linearized potential functions defined in 2.1

$$\nabla^2\Phi = 0 \tag{2.15}$$

and the non-penetrating condition is defined as null normal velocity (defined as the potential gradient) on the body surface:

$$\nabla\Phi \cdot \boldsymbol{n} = 0 \tag{2.16}$$

The Green function is exploited to formulate the potential problem. Having defining the generic quantity $\boldsymbol{q}$, and considering it's product to the normal of a generic surface, the divergence theorem can be exploited:

$$\int_S \boldsymbol{n} \cdot \boldsymbol{q} dS = \int_V \nabla \cdot \boldsymbol{q} dV \tag{2.17}$$

For the case considered, said generic quantity can be replaced by:

$$\Phi_1\nabla\Phi_2 - \Phi_2\nabla\Phi_1 \tag{2.18}$$

where Φ_i is a position scalar function. Applying the divergence theorem the following is obtained:

$$\int_S (\Phi_1\nabla\Phi_2 - \Phi_2\nabla\Phi_1) \cdot \boldsymbol{n} dS = \int_V \nabla(\Phi_1\nabla^2\Phi_2 - \Phi_2\nabla^2\Phi_1) dV \tag{2.19}$$

Defining:

$$S = S_B + S_w + S_\infty \qquad \text{where } S_B, S_w, S_\infty \text{ are body, wake and boundary surfaces}$$

$$V \qquad \text{is the control volume}$$

$$\Phi_1 = \frac{1}{r} \qquad \text{where } r \text{ is the distance from a point } P(x, y, z)$$

$$\Phi_2 = \Phi \qquad \text{is the velocity potential of the flow in the control volume}$$

and excluding the point $P(x, y, z)$ from the integration region, by surrounding it with a sphere of radius ϵ, equation 2.19 becomes:

$$\int_{S+S_\epsilon} (\frac{1}{r}\nabla\Phi - \Phi\nabla\frac{1}{r}) \cdot \boldsymbol{n} dS = 0 \tag{2.20a}$$

and considering the sphere normal pointing inward:

$$-\int_{S_\epsilon}(\frac{1}{r}\frac{\partial\Phi}{\partial r}-\frac{\Phi}{r^2})dS+\int_S(\frac{1}{r}\nabla\Phi-\Phi\nabla\frac{1}{r})\cdot\boldsymbol{n}dS=0 \tag{2.20b}$$

When considering the sphere surrounding P, $\int dS = 4\pi\epsilon^2$, which enables us to rewrite the second term of the sphere integral as a potential of point P.
Equation 2.20b becomes:

$$\Phi(P)=\frac{1}{4\pi}\int_S(\frac{1}{r}\nabla\Phi-\Phi\nabla\frac{1}{r})\cdot\boldsymbol{n}dS \tag{2.21}$$

Taking equation 2.21 and applying the following hypotesis:

$$\Phi(P)=\frac{1}{4\pi}\int_{S_B,S_w,S_\infty}(\frac{1}{r}\nabla\Phi-\Phi\nabla\frac{1}{r})\cdot\boldsymbol{n}dS \tag{2.22a}$$

$$\frac{1}{4\pi}\int_{S_B}(\frac{1}{r}\nabla\Phi_i-\Phi_i\nabla\frac{1}{r})\cdot\boldsymbol{n}dS=0 \text{ with } i \text{ inside the body} \tag{2.22b}$$

$$\frac{\partial\Phi}{\partial n}=0 \text{ on the wake} \tag{2.22c}$$

Equation 2.21 can be rewritten as

$$\Phi(P)=\frac{1}{4\pi}\int_{S_B}(\frac{1}{r}\nabla(\Phi-\Phi_i)-(\Phi-\Phi_i)\nabla\frac{1}{r})\cdot\boldsymbol{n}dS-\frac{1}{4\pi}\int_{S_w}\nabla\boldsymbol{n}\cdot\frac{1}{r}dS+\Phi_\infty(P) \tag{2.23}$$

This equation reduces the potential evaluation to the boundaries of the problem. For each section of the boundary, a source and doublet intensity can be defined. The unit source intensity is defined as:

$$-\sigma=\frac{\partial\Phi}{\partial n}-\frac{\partial\Phi_i}{\partial n} \tag{2.24}$$

while the doublet unit intensity is defined as:

$$-\mu=\Phi-\Phi_i \tag{2.25}$$

Then equation 2.23 is can be written as a combination of sources and doublets distributed on the boundary S_b:

$$\Phi(x,y,z)=\frac{-1}{4\pi}\int_{S_b}\left[\sigma\left(\frac{1}{r}\right)-\mu\boldsymbol{n}\cdot\nabla\left(\frac{1}{r}\right)\right]dS+\Phi_\infty \tag{2.26}$$

2.2.2. Problem formulation and boundary conditions

As discussed in the previous sections, a combination of sources and doublets can be used to represent thick and lifting bodies. Considering the following body:

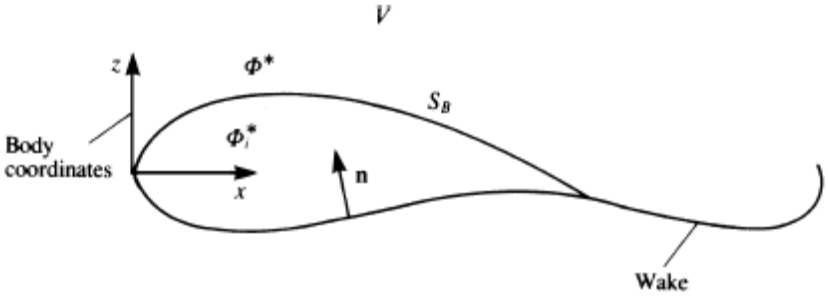

Figure 2.1: Reference body, wake and normal (form [16])

the thickness problem can be represented by a combination of sources σ, while the lifting components included in the body and the wake can be represented by a combination of doublets μ, as shown in equation 2.27

$$\Phi(x,y,z) = -\frac{1}{4\pi}\int_{body}\sigma\left(\frac{1}{r}\right)dS + \frac{1}{4\pi}\int_{body+wake}\mu\boldsymbol{n}\cdot\nabla\left(\frac{1}{r}\right)dS + \Phi_\infty \tag{2.27}$$

Achieve an unique solution for the problem, the non penetration boundary condition has to be imposed on the body surface. Two type of boundaries conditions can be imposed:

$$\left.\frac{\partial\Phi^*}{\partial n}\right|_{S_b} = 0 \qquad \textit{Neumann Boundary Condition} \tag{2.28a}$$

$$\nabla(\Phi^* + \Phi_\infty)\cdot\boldsymbol{n}|_{S_b} = 0 \qquad \textit{Dirichlet Boundary Condition} \tag{2.28b}$$

The former directly poses a potential derivative at the surface boundary S_b equal to zero, thus exploiting the null normal velocity at the boundary, imposing the non penetration boundary condition. The latter specifies a potential Φ^* such that the non penetration condition is indirectly satisfied. In the numerical implementation of this thesis the latter is chosen as imposing method, being suited for numerical implementation of a linear system.
Setting equation 2.28b equal to Φ_∞, equation 2.27 can be rewritten as:

$$-\frac{1}{4\pi}\int_{body}\sigma\left(\frac{1}{r}\right)dS + \frac{1}{4\pi}\int_{body+wake}\mu\frac{\partial}{\partial n}\left(\frac{1}{r}\right)dS = 0 \tag{2.29}$$

which, rearranged and combined to the Neumann formulation in equation 2.28a, leads to the

non penetration formulated as:

$$\sigma = \boldsymbol{n} \cdot \boldsymbol{Q}_\infty \tag{2.30}$$

The final step for achieving an unique solution, characteristic of each geometry, is to determine the circulation intensity. From figure 2.3 the circulation can be represented as a closed vortex line.

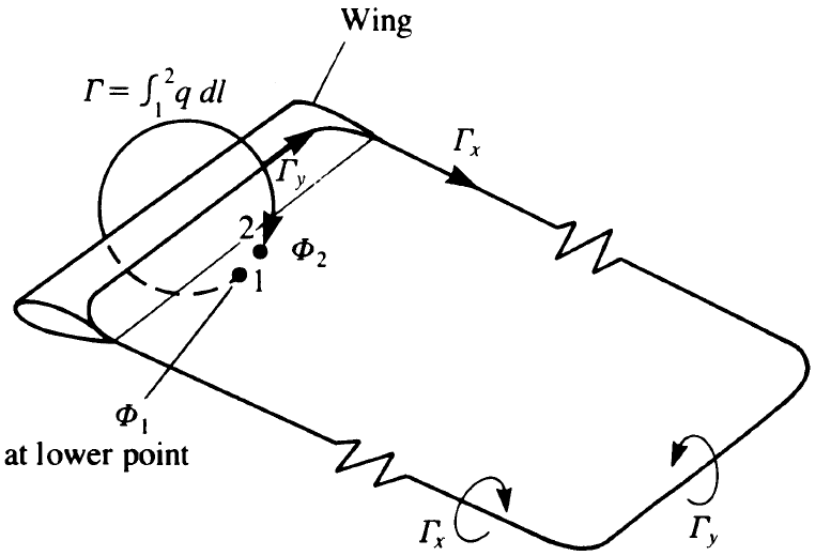

Figure 2.2: Circulation intensity (from [16])

This leads to a discontinuity in the velocity potential at the trailing edge, which can be defined as:

$$\Gamma = \oint_1^2 \boldsymbol{q} \cdot dl = \Phi_2 - \Phi_1 \tag{2.31}$$

To properly model the Kutta condition, a null circulation at the trailing edge has to be imposed. This can be expressed as:

$$\gamma_{T.E.}(s) = -\frac{\partial \mu}{\partial s} \tag{2.32a}$$

which leads to

$$\mu_{T.E.} = \mu_W = cost \tag{2.32b}$$

Having determined a relation between the body doublets intensity and the wake doublets intensity, the problem becomes a function of the body doublets intensity only. For a time stepping method, the wake doublet intensity is changed only for the latest shed panel. This change describes the variation of the profile circulation, and subsequently the produced lift. This changes the solved system, as explained in the next section.

2.2.3. Doublet source paneling

To build the AIC (Aerodynamic Influence Coefficient) matrices the method proposed by Katz and Plotkin ([16]) is used, which is derived from the work of Hess and Smith ([13]).

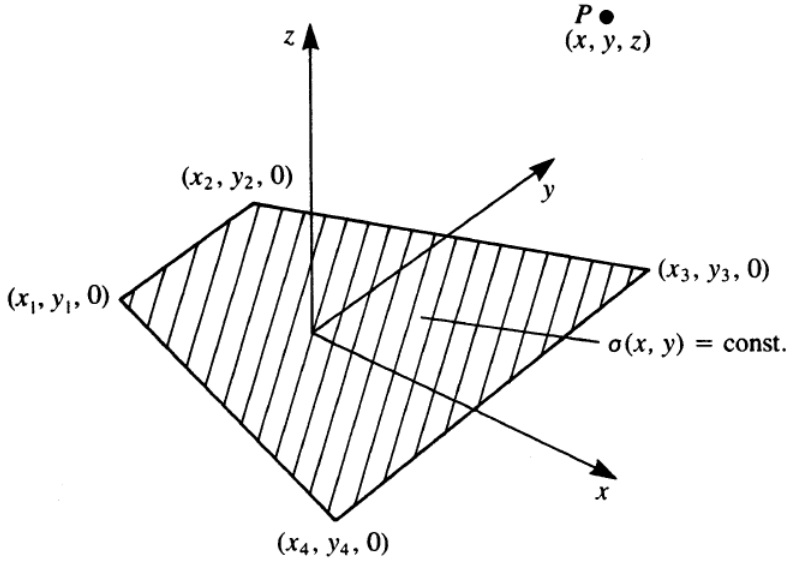

Figure 2.3: Panel element (from [16])

A combination of constant sources and doublets is used to model the profile surface. The influence of a single panel on an arbitrary point P is computed as:

$$\Phi(x,y,z) = \frac{-\sigma}{4\pi}\int_S \frac{dS}{\sqrt{(x-x_0)^2+(y-y_0)^2+z^2}} \text{ is the source potential} \tag{2.33a}$$

$$\Phi(x,y,z) = \frac{-\mu}{4\pi}\int_S \frac{zdS}{[(x-x_0)^2+(y-y_0)^2+z^2]^{\frac{3}{2}}} \text{ is the doublet potential} \tag{2.33b}$$

Before computing the panel influence on the point the latter has to be moved to the former local frame of reference, in order to avoid the presence of numerical errors due to erroneous computation of the point distance. If the external flow conditions and wake shape are not subjected to variations, the value of the influence coefficients remains constant, leading to constant sources intensities and doublets values. Equation 2.33b is used to compute, using an unit intensity doublet panel, the influence coefficient of a panel element on a given point, the latter being the collocation point of any geometry panel. This computation is repeated for every panel element, leading to a $N \times N$ system of influence coefficients, where N is the number of panels discretizing the geometry. Equation 2.33a is applied in the same way, this time computing the influence coefficient of a unit intensity source panel, and another $N \times N$ system is obtained. Operat The

presence of at least one wake panel, in order to enforce the Kutta condition and achieving lift production, would lead to an unsolvable system, having to compute the wake panel doublet intensity, which would lead to an array of unknowns of dimension $N + 1$. To solve this problem, and express the wake doublets intensity as a function of the body doublets intensity, the intensity of the former is computed as the difference of the upper and lower trailing edge panels doublets, i.e. $\mu_W = \mu_{T.E.} = \mu_{UP} - \mu_{LOW}$. Having established this relation, the influence coefficients of the wake panels can be computed applying Eq. 2.33b (Eq. 2.33a is not applied, being the wake a doublets sheet), and the computed coefficients are added to the linear system in the columns corresponding to the doublets intensities used to obtain the relation between body and wake. For the unsteady system, the computation of the wake influence coefficients is done by computing the influence of the wake panels not connected to the trailing edge. Those coefficients are stored in a different matrix with size $N \times M - 1$, where M is the timestep number. The corresponding doublets intensities are recovered from previous computations, hence all the terms related to the wake are known. The following linear system is obtained:

$$\begin{bmatrix} a_{1,1} & \cdots & a_{1,n} \\ a_{2,1} & \cdots & a_{2,n} \\ \vdots & \ddots & \vdots \\ a_{n,1} & \cdots & a_{n,n} \end{bmatrix} \begin{Bmatrix} \mu_1 \\ \mu_2 \\ \vdots \\ \mu_n \end{Bmatrix} = \begin{bmatrix} b_{1,1} & \cdots & b_{1,n} \\ b_{2,1} & \cdots & b_{2,n} \\ \vdots & \ddots & \vdots \\ b_{n,1} & \cdots & b_{n,n} \end{bmatrix} \begin{Bmatrix} \sigma_1 \\ \sigma_2 \\ \vdots \\ \sigma_n \end{Bmatrix} + \begin{bmatrix} a_{w_{1,1}} & \cdots & a_{w_{1,n_w}} \\ a_{w_{2,1}} & \cdots & a_{w_{2,n_w}} \\ \vdots & \ddots & \vdots \\ a_{w_{n,1}} & \cdots & a_{w_{n,n_w}} \end{bmatrix} \begin{Bmatrix} \mu_{w_1} \\ \mu_{w_2} \\ \vdots \\ \mu_{w_n} \end{Bmatrix} \tag{2.34}$$

The only unknown in the system 2.34 is the column vector containing the body doublets intensities μ_i, being the wake doublets intensities μ_{w_i}referring to the previous time step body doublets, and hence known, and the sources intensities σ_i computed as described in Eq. 2.30. For the latter, each panel normal is considered and is multiplied by the free-stream velocity, obtaining the source intensity $\sigma_i = \vec{n}_i \cdot \vec{U_\infty}$. Combining the terms in the right-hand-side, by multiplying each coefficients matrix to the corresponding known quantities, a column vector is achieved, and the whole problem can be rewritten as a linear system in the form:

$$A\vec{x} = b \tag{2.35}$$

The solution vector contains each panel circulations, which are then used to compute the forces acting on the wing. Being the wing discretized in panels, the local velocities on each panel are computed using the centered difference method, using the adjacent panels to the considered one. In equations 2.36.i the computed quantities are, in order, the local chord-wise velocity, the local span-wise velocity and the local normal velocity.

$$q_u = \frac{\mu_{i+1,j} - \mu_{i-1,j}}{dx} \tag{2.36a}$$

$$q_l = \frac{\mu_{i,j+1} - \mu_{i,j-1}}{dy} \tag{2.36b}$$

$$q_n = -\sigma_{i,j} \tag{2.36c}$$

The normal velocity component for the singular panel is computed using the source intensity. This exploits the superposition of elementary flows, which is a result of the linearization described in the previous section. Once the local velocity components are computed as

$$U(i,j) = (U_\infty \cdot \hat{\mathbf{t}} - q_u) + (U_\infty \cdot \hat{\mathbf{l}} - q_l) + (U_\infty \cdot \hat{\mathbf{n}} - q_n) \tag{2.37}$$

where $\hat{\mathbf{t}}$ is the panel local tangential vector (i.e. the one pointing chord-wise), $\hat{\mathbf{l}}$ is the panel local longitudinal vector (i.e. the one pointing span-wise) and $\hat{\mathbf{n}}$ is the panel local normal vector. The C_p value for each panel is computed as:

$$C_p(i,j) = 1 - \frac{||U_{i,j}^2||_2}{||{U_\infty}^2||_2} \tag{2.38}$$

If an unsteady problem is considered, the time variation of the panel circulation has to be considered, adding to equation 2.37:

$$C_p(i,j) = 1 - \frac{||U_{i,j}^2||_2}{||{U_\infty}^2||_2} - \frac{2}{||{U_\infty}^2||_2}\frac{\mu_t - \mu_{t-1}}{dt} \tag{2.39}$$

The computations in Eq. 2.37 and Eq. 2.39 are to be modified in order to take into account the induced velocities by the leading edge vortices. This will be described in Section 2.2.5. Having computed the C_p distribution on the wing the principal forces and moments can be computed, as well as the characterizing aerodynamic coefficients of the analyzed wing. The dynamic pressure on each panel is computed, resulting in three force components for each panel:

$$q_{D_{i,j}} = \frac{1}{2}\rho U_\infty^2 \cdot C_p(i,j) \tag{2.40a}$$

$$dF_{x,y,z}(i,j) = -q_{D_{i,j}} S_{i,j} \hat{\mathbf{n}}_{x,y,z} \tag{2.40b}$$

$$L = \sum_{i=1}^{N} dF_{x_i} \sin\alpha - dF_{z_i} \cos\alpha \tag{2.40c}$$

$$D = \sum_{i=1}^{N} dF_{x_i} \cos\alpha + dF_{z_i} \sin\alpha \tag{2.40d}$$

The following algorithms are used to compile the aerodynamic influences matrices. The body

panels influence coefficients are computed as stated in Algorithm 2.1, and the result is stored in the pre-allocated matrices.

Algorithm 2.1 Influence coefficients computation

for $i = 1{:}N_{PANELS}$ **do**
  for $j = 1 : N_{PANELS}$ **do**
    Select i^{th} panel
    Select j^{th} panel collocation point
    Call source-doublet panel coefficients computation routine
    Assign values to doublets (unknowns) and sources (known) matrices A(i,j) and B(ij)
  end
end

The same loop is repeated for the wake panels, for which the source influence is not computed, being the wake modelled as a doublet sheet, as stated above. For the steady system wake aerodynamic influence matrix, only the computation of the first wake panel is required, having to impose the Kutta condition. This is done by executing 2.1 using as influencing panels the wake panels. This lead to an $N \times M$ matrix, with N being the number of panels and M the number of trailing edge panels. The influence coefficients are then added to the body AIC matrix to the columns corresponding to each section upper and lower trailing edge panel:

Algorithm 2.2 Kutta condition application

for $i = 1{:}N_{SPANSECTIONS}$ **do**
  for $j = 1 : N_{PANELS}$ **do**
    Select i^{th} section trailing edge panels indices
    Define upper panel with UP index
    Define lower panel with LP index
    Select i^{th} section first wake panel
    Select j^{th} panel collocation point
    Call doublet panel coefficients computation routine
    Add coefficient to matrix A in i^{th} row and UP column, A(i,UP)
    Subtract coefficient to matrix A in i^{th} row and LP column, A(i,LP)
  end
end

Having defined the influeces matrices, the system can be solved and the forces acting on the wing can be computed.

2.2.4. Vortex filament induced velocity

To compute the velocity induced by a vortex line the Biot-Savart line integral is used:

$$q = \frac{\Gamma}{4\pi}\int_l \frac{d\mathbf{l}\times\mathbf{r}}{r^3} \tag{2.41}$$

The derivation of the induced velocity will not be reported in this text (it is properly explained in [16]). This formulation poses the problem of producing nonphysical results when approaching the vortex core. When $r \to 0$ the induced velocity tends to infinity. Being the core of this work the modelling of interaction between free-vortex and body surface induced velocity, the vortex core model is introduced. The proposed models are the following, in accordance with what is proposed by Hommes *et al.* [14]. First, the a-dimensional tangential velocity is defined as function of the computed velocity and the vortex core radius r_v: $\bar{V}_\theta = V_\theta/\Gamma 2\pi r_v$. The a-dimensional distance is defined as: $\bar{r} = \frac{r}{r_v}$. Then the different core models are defined as:

Rankine
$$\bar{V}_\theta = \begin{cases} \bar{r} & \bar{r} < 1 \\ \frac{1}{\bar{r}} & \bar{r} > 1 \end{cases} \tag{2.42a}$$

Lamb-Oseen
$$\bar{V}_\theta = \frac{1}{\bar{r}}(1 - e^{-1.2526\bar{r}^2}) \tag{2.42b}$$

Burnham-Hallock
$$\bar{V}_\theta = \frac{\bar{r}}{\bar{r}^2 + 1} \tag{2.42c}$$

Proctor
$$\bar{V}_\theta = \begin{cases} \frac{1}{\bar{r}}(1 - e^{(-\beta(1/\bar{B})^{0.75}})(1 - e^{-1.2526\bar{r}^2}) & \bar{r} < 1 \\ \frac{1}{\bar{r}}(1 - e^{(-\beta(1/\bar{B})^{0.75}}) & \bar{r} > 1 \end{cases} \tag{2.42d}$$

Proctor-Winckelmans
$$\bar{V}_\theta = \frac{1}{\bar{r}}(1 - exp(-\beta(1/\bar{B})^2)/(1 + (\beta_i/\beta_0)(\bar{r}/\bar{B})^{1.2})^p)^{1/p}) \tag{2.42e}$$

Jacquin
$$\bar{V}_\theta = \begin{cases} \bar{r}/\bar{r}_0^{0.5} & \bar{r} \le 1 \\ 1/(\bar{r}\bar{r}_0)^{0.5} & 1 < \bar{r} \le \bar{r}_0 \\ \frac{1}{\bar{r}} & \bar{r} > 1 \end{cases} \tag{2.42f}$$

Vatistas
$$\bar{V}_\theta = \frac{\bar{r}}{(\bar{r}^{2n} + 1)^{1/n}} \tag{2.42g}$$

It should be noted that each model was mathematically manipulated to better suit the required numerical implementation The models were replicated to have a better insight in the vortex phenomenology:

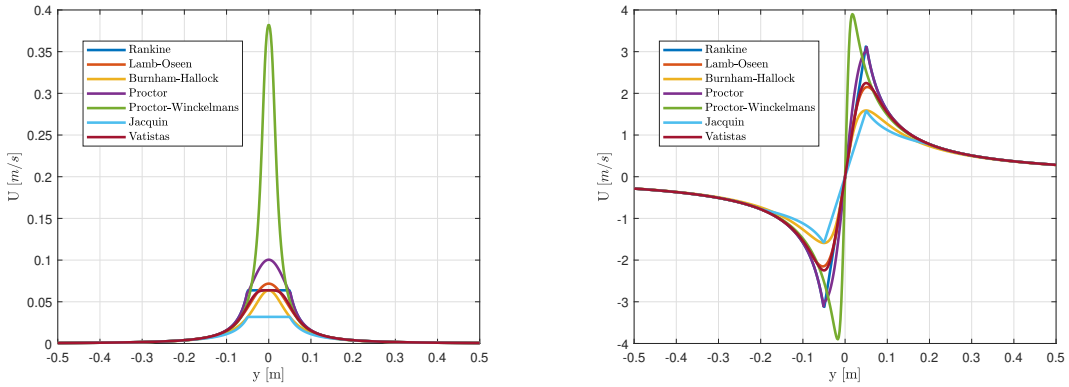

(a) v component for different core models.

(b) w component for different core models.

Figure 2.4: Vortex core models comparison

As shown in Figure 2.4 each model proposes a different interpolation from the vortex axis up to the end of the vortex core, whose radius, in this case, is set to $r_v = 0.05$. To test the numerical implementation of the vortex line, a test case was set-up: a number of points would progressively approach the vortex line, and the resulting induced velocity is computed.

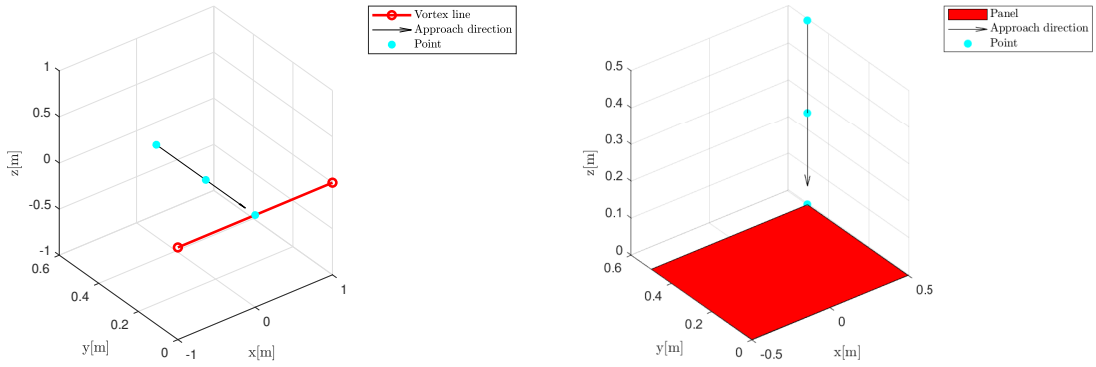

(a) Vortex line test cases.

(b) Doublet panel test case.

Figure 2.5: Vortex models test cases

The implementation of a modelled core is crucial for a correct computation of induced velocities, as shown in Figure 2.6 The line representing the un-modelled core, as expected, tends to infinity when approaching the vortex axis. This could lead to incorrect velocities prediction, if the vortex were to be too close to the point of interest. The implementation of a core model solves this problem, with the velocity reaching linearly (if Rankine or Jacquin model are chosen) decreasing to 0 when the point of interest is within the vortex core.

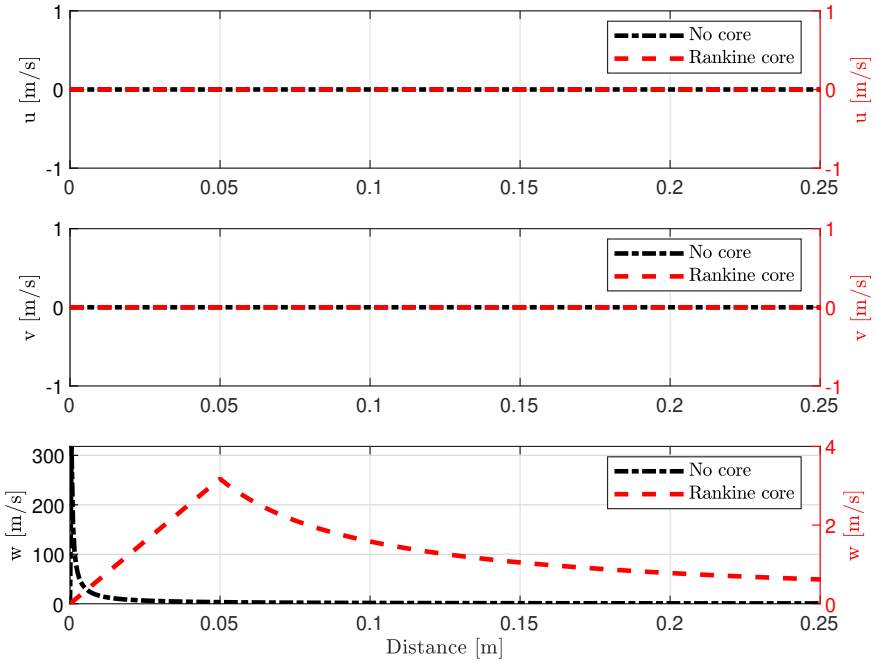

Figure 2.6: Induced velocities comparison. Rankine core model is used

A similar test case was setup to evaluate the implementation of the induced velocity for a doublet panel. Being a double panel comparable to a vortex panel ([16]), a similar methodology of induced velocity computation can be used. This becomes particularly useful when computing velocities induced by wake panels, as is the case of wake roll-up estimation. In this case the comparison is made between a simple doublet panel and a doubet-source panel combination. The latter is implemented to evaluate the induced velocity by a solid body (i.e. a wing test section).

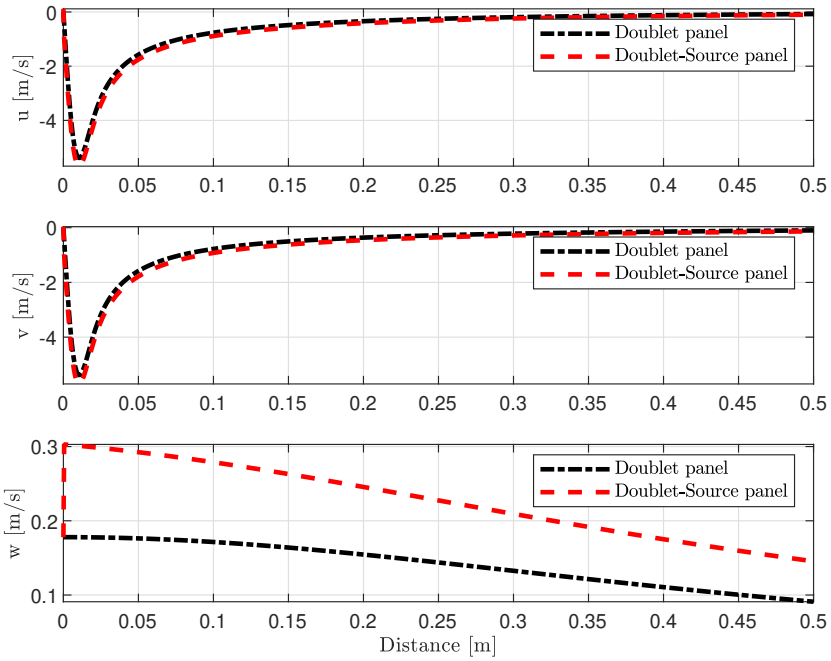

Figure 2.7: Induced velocities comparison. Vasistas core model is used

Two results are particularly worth of noting:

1. The rotational velocities are analogous to the ones computed considering a single vortex line.
2. Being the velocity computed at the panel corner, the rotational component of the velocity is induced in two normal directions, being influenced by two perpendicular vortices.
3. A third velocity component originates from this interaction of the 4 vortices. If the panel is to be considered a source panel as well, the source induces a constant velocity output, producing a velocity offset compared to the sole doublet.

Having verified the modelling of the vortex, its influence on a whole plane is analyzed. Three different cases are analyzed:

1. Single vortex.
2. Two counter rotating vortices.
3. Two counter rotating vortices with mirror images to emulate wall proximity.

The first test case is defined as follow: a singular vortex segment is intersected by a computation mesh. On each node of the mesh the induced velocity by the vortex is calculated.

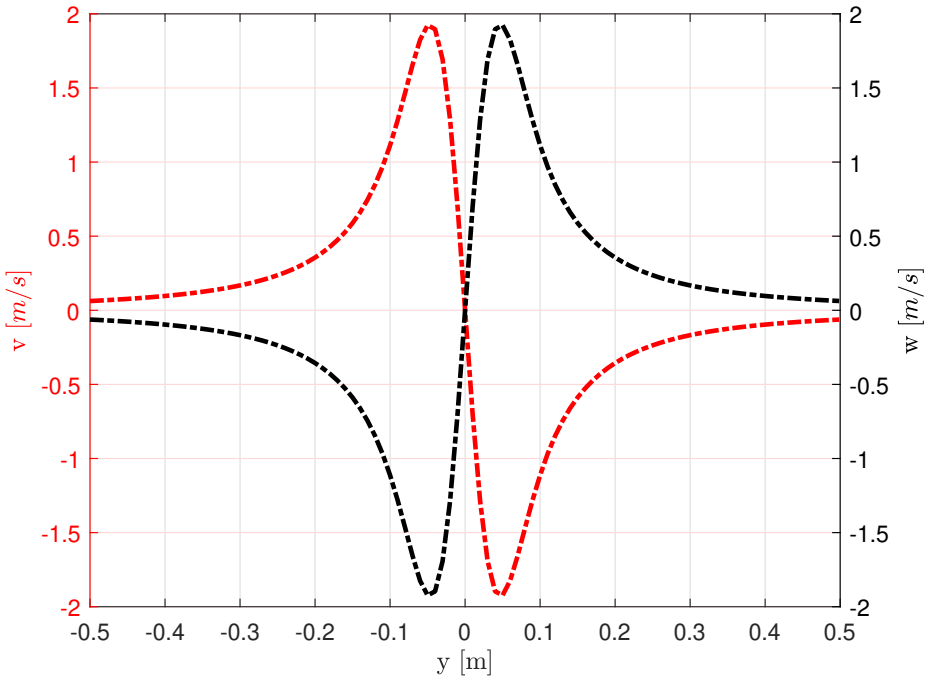

(a) Induced velocity magnitude.

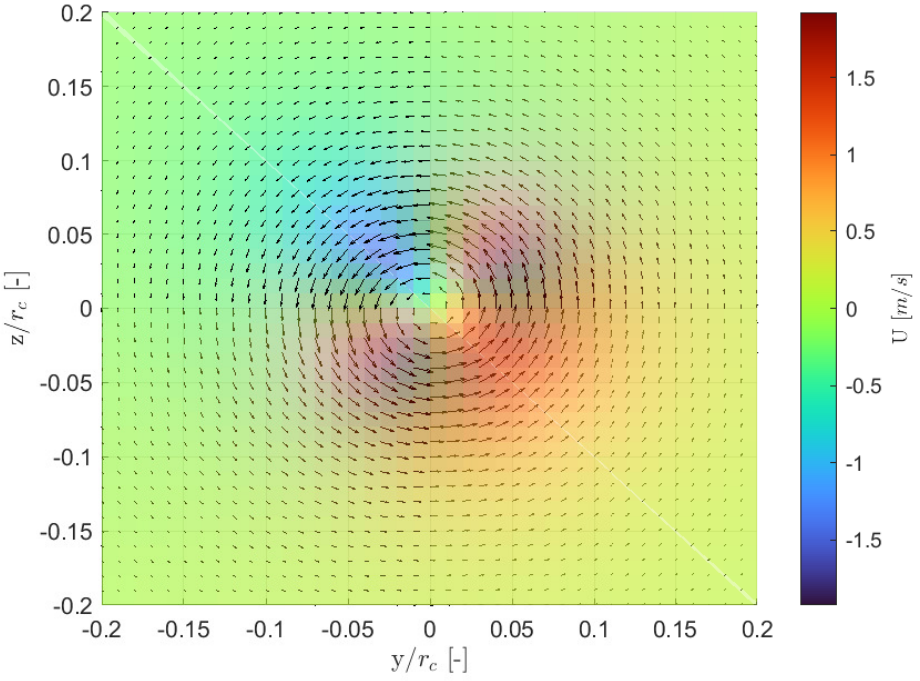

(b) Induced velocity direction.

Figure 2.8: Single vortex induced velocities

In this case, the velocities in y and z direction are symmetric, which is coherent with the vortex

model. In figure 2.9 the computed results are compared with the measured velocity by [14].

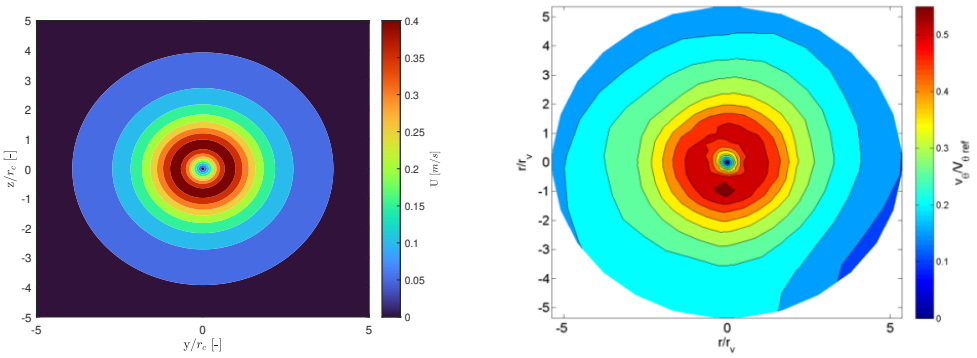

(a) Computed induced velocity. (b) Measured induced velocity ([14]).

Figure 2.9: Induced velocities comparison

It's interesting to notice an axial asymmetry in the measured velocity, with the velocity decay mitigated in the lower-left quadrant. This phenomena is not modelled in this work. This effect is deemed of lower order compared to the overall influence of the vortex model. This would require, on the other hand, a consistent increase in the programming and computational effort for a minor benefit in the physical description. The second test was carried on two counter rotating vortices to asses their interaction and subsequent induced velocity. For Figure 2.10a a mid-plane cutting through the vortices cores is considered. The velocity plotted validates what seen with the single vortex core, with the two velocity fields blending smoothly and avoiding reaching the detrimental core singularity. Considering the velocity quivers reported in Figure 2.10b, the counter rotating vortices have the effect of accelerating the particles between their axis, producing the effect described by the vortices introduced in Chapter 1. This is further validated by the velocities computed by the pair of vortices with counter images, reported in Figure 2.11. The vortex operating close to the solid boundary (in this case modelled with the specular vortices, in the actual case modelled by the wing solid surface) further enhances the induced velocity. The chosen core model is the Vatistas, due to is good approximation of induced velocity, as defined by [14].

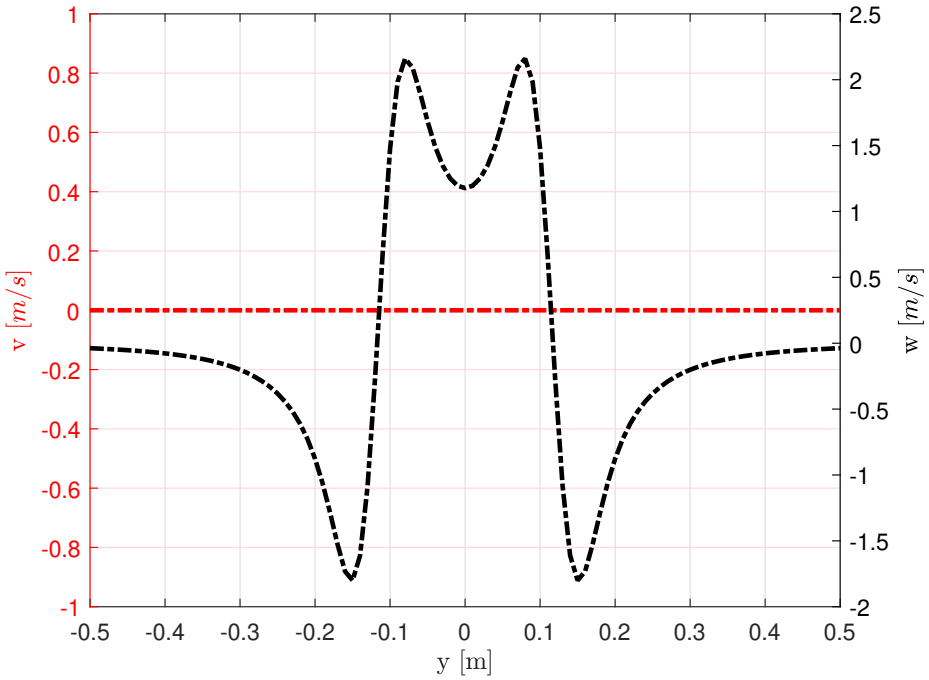

(a) Induced velocity magnitude.

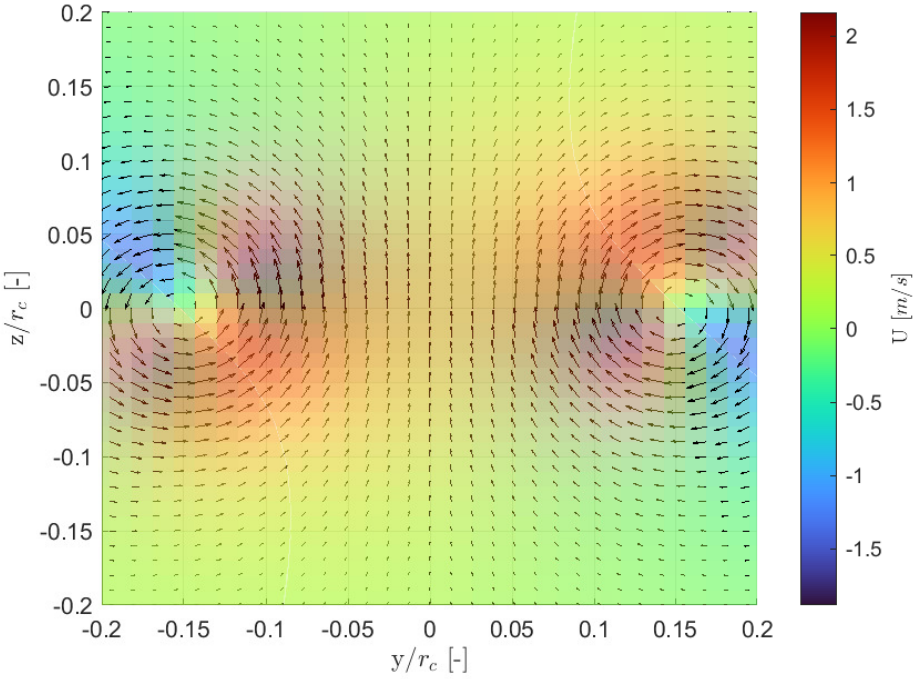

(b) Induced velocity direction.

Figure 2.10: Counter rotating vortices induced velocities

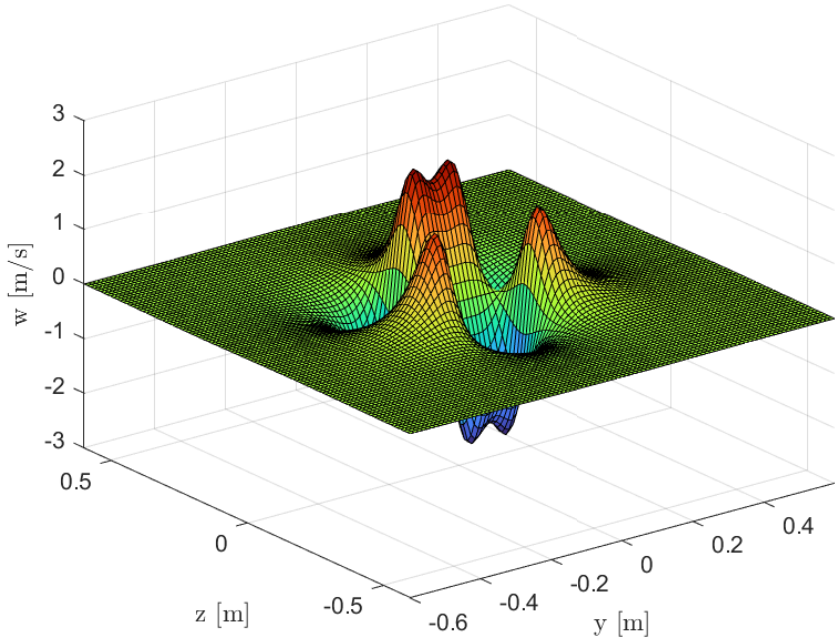

(a) Induced velocity magnitude.

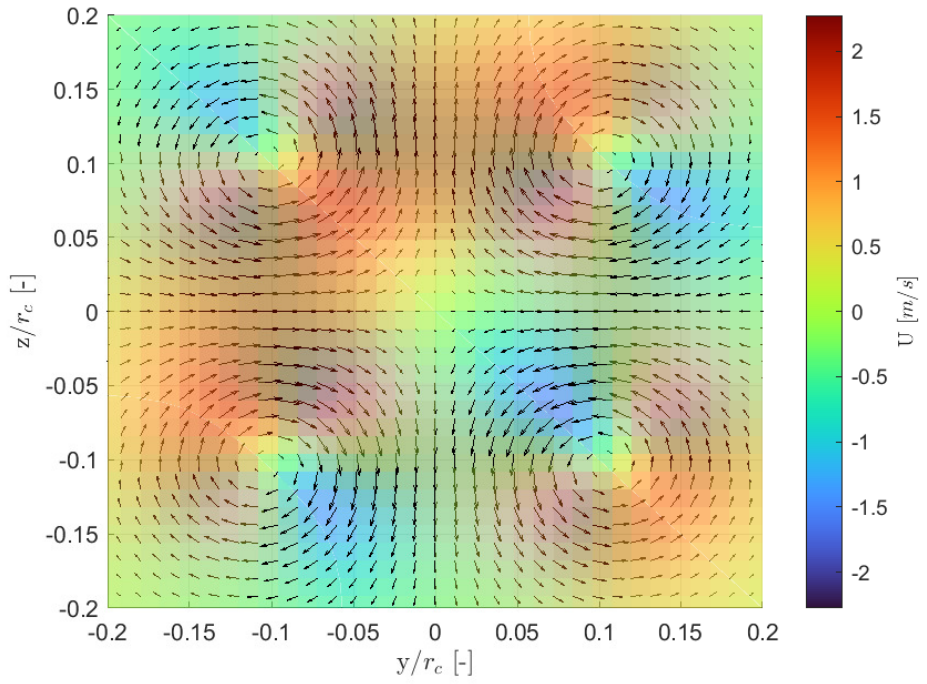

(b) Induced velocity direction.

Figure 2.11: Counter rotating vortices with image induced velocities

2.2.5. Leading edge vortices

Having defined the physical modelling of the vortex line, and its adaptation to avoid numerical singularities, the line is added to the developed numerical solver by implementing the following modifications:

- Vortex initialization: the vortex line is shed from a body panel, modelling the generation of the leading edge vortex
- Vortex motion: the vortex motion along the wing suction side is modelled to progressively depart from the surface, as demonstrated by experimental evidence (Kim *et al.* [18]).

The tuned parameters to model the vortex motion were the point of detachment from the suction side, i.e. where the leading edge vortex is originated, and the displacement from the wing surface, i.e. how much the vortex departs from the surface while progressing in the chord-wise direction. The former is realized by geometrical analysis of the wing in exam. The tubercles are generated by means of harmonic functions, such as

$$y(x) = A sin(\frac{2\pi}{\lambda}x) \tag{2.43}$$

where y is the delta applied to the straight leading edge coordinate, x is the span-wise coordinate, A is the tubercle amplitude, define as percentage of the chord, and λ is the tubercle wavelength, defined as percentage of the chord as well. Having defined the leading edge geometry, generated the wing panels, the index indicating the panels corresponding to the geometrical trough are stored. These indices are then used to call the geometrical coordinates corresponding to the panels which are located along the trough section. Having fetched the nodes, these are manipulated to obtain the free-vortices nodes. The following process is used:

1. Determine vortex starting point: the starting point along the chord is determined as chord percentage. To fit the experimental evidence, the starting point is chosen at point $P = 0.25c$
2. Fetch remaining nodes along the section of interest: the remaining nodes from the starting point to the trailing edge are stored.
3. Translate nodes from wing surface: the section nodes are duplicated and moved along the y-axis in opposite directions and progressively moved from the axis. The following relation is used to translate the nodes:

$$P_{V.L.}(x, y, z) = \vec{x}\, d\, i\, P_i(x, y, z) \tag{2.44}$$

where d is the offset parameter, i is the node number (which increases from node to node along the section), P_i is the node original coordinate and $P_{V.L.}$ is the final node coordinate. For the y-axis translation, the chosen distance is corresponding to a quarter of the wavelength λ.

The resulting vortices can be seen in Figures 2.12 and 2.13, where the isometric and side views are shown.

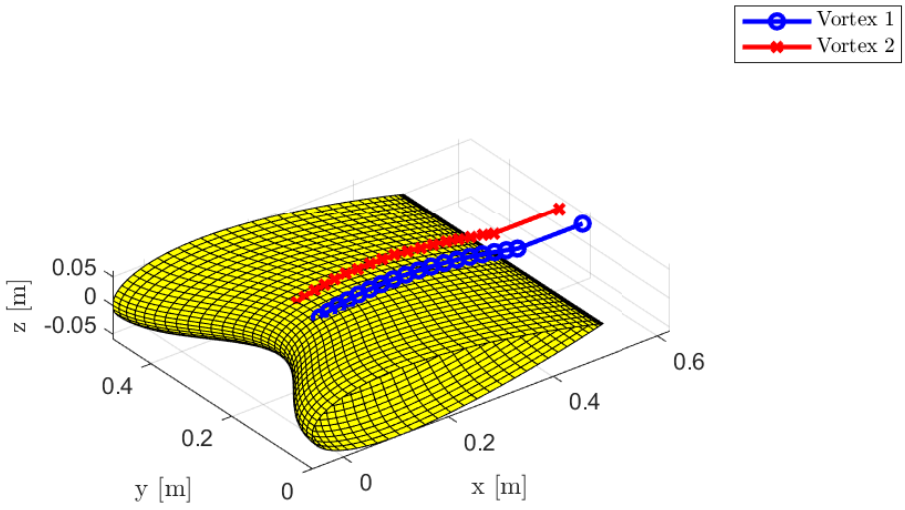

Figure 2.12: Leading edge vortices

The vortex lines do depart from the wing surface, and when reaching the trailing edge it is aligned with the free-stream. The geometry of the vortices are tuned to fit the results described by Hansen *et al.* ([12]). A thorough description of the wing modelled will be given in Chapter 4. Having defined the vortices geometry, the corresponding doublet intensity is determined. This is done by assigning to the vortex line the doublet intensity of the corresponding panel, so that

$$\Gamma_i = \mu_{PANE} \tag{2.45}$$

where Γ_i is the circulation of the i^{th} vortex and μ_{PANE} is the intensity of the corresponding panel. This provides the needed term to compute the induced velocities by the line. This is achieved by using the relations defined in Paragraph 2.2.4. A critical aspect is to determine the side on which the vortices are shed, being dependent on the angle of incidence of the wing. To determine the side of shedding, after the solution of the linear system describing the condition

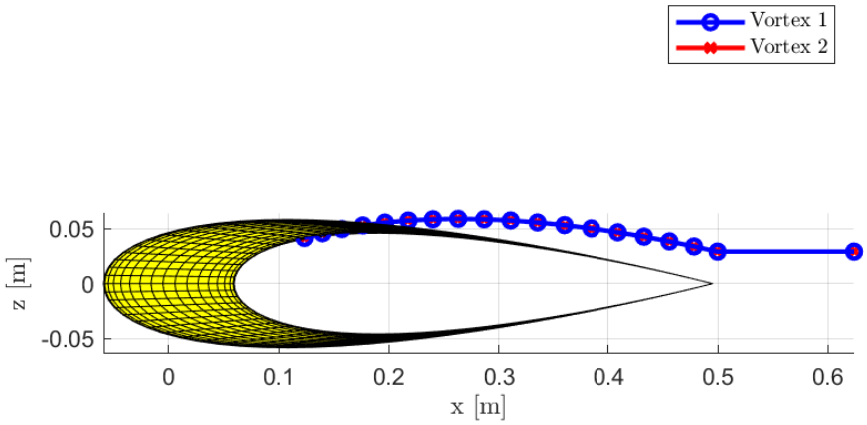

Figure 2.13: Leading edge vortices, side view

analyzed, doublets intensity is determined. The surface forces acting on the wing are computed and, once the suction side its defined, the intensity of this side doublets are assigned to the corresponding vortices. Surface forces are then recomputed, this time including the induced velocities contribution defined by the free-vortices. The description of the process is given in Algorithm 2.3.

Algorithm 2.3 Vortex induced velocities

Solve linear system → Determine surface doublets

Compute surface C_p → Determine suction side

Fetch doublets intensities→Assign intensities to corresponding vortices

for $i = 1{:}N_{PANELS}$ **do**

  for $j = 1 : N_{VORTEX}$ **do**

    Select i^{th} panel

    Select j^{th} vortex

    Compute the induced velocity by the j^{th} vortex on the i^{th} panel

    Add the velocity to the C_p computation determine pressure distribution with the vortices effect.

  end

end

Recompute surface forces with vortex lines contribution→Move to next iteration

To account for the additional velocity contribution, Equation 2.37 is modified as:

$$U(i,j) = (U_\infty \cdot \hat{\mathbf{t}} - q_u + u_{ind}) + (U_\infty \cdot \hat{\mathbf{l}} - q_l + v_{ind}) + (U_\infty \cdot \hat{\mathbf{n}} - q_n + w_{ind}) \tag{2.46}$$

This representation of the vortices was chosen for the following reasons:

- Flexibility: the relation between vortex intensity, geometry and corresponding surface ensures a high degree of customization, allowing to tailor the vortex positioning to each wing geometry and flow case
- Robustness: instead of applying a numerical correction to the planform results in order to fit experimental data, which would be highly dependant on the experimental conditions, this modelling should provide a good degree of representation of the actual flow condition
- Computational expense: other methodologies considered included the modelling of a leading edge wake with wake roll-up, and a numerical dampening of the wing C_L. However those methodologies presents, for the former a considering programming effort, with the risk of nonphysical solutions (due to wake roll-up), and extensive computational times, due to the increased number of panels required. The latter, on the other hand, presents a strong limitation in physical representation of the phenomena. The vortex line solution, on the other hand, was quick to implement and closely recalling the actual phenomena observed.

2.2.6. Theodorsen approximation

The Theodorsen model, as described in [3], is an extension of the quasi-steady model of the thin airfoil theory. The quasi-steady model can be written as:

$$C_L^{QS} = 2\pi\left[\alpha + \dot{h} + \dot{\alpha}\left(\frac{1}{2} - a\right)\right] \tag{2.47}$$

where α is the wing angle of attack, $\dot{h}$ is the wing plunge velocity, $\dot{\alpha}$ is the pitching velocity and a is the nondimensionalized pitch axis position, where $a = -1$ is the Leading Edge and $a = 1$ is the Trailing Edge.

When the Theodorsen approximation is considered, the addition of further terms has to be considered to correctly model the added-mass terms depending on the wing acceleration and the lift production dissipation due to wake effects. The former is achieved by adding the mass terms to 2.47, the latter by multiplying 2.47 by a transfer function. Theodorsen's transfer function $C(k)$ is expressed in term of the Hankel functions, which itself are expressed in form of Bessel functions:

$$C(k) = \frac{H_1^{(2)}(k)}{H_1^{(2)}(k) + jH_0^{(2)}(k)} \tag{2.48}$$

By modifying the proposed equations 2.47, the full unsteady Theodorsen Lift equation is achieved:

$$C_L = \pi\left[\ddot{h} + \dot{\alpha} - a\ddot{\alpha}\right] + 2\pi\left[\alpha + \dot{h} + \dot{\alpha}\left(\frac{1}{2} - a\right)\right]C(k) \tag{2.49}$$

The k term is the imaginary part of the reduced frequency, which is derived from the angular frequency ω as:

$$k = b\omega/U_\infty \tag{2.50}$$

where b is the reference length and U_∞ is the free-stream flow velocity. By applying the Laplace transformation to 2.49, the C_L and C_M equations can be rewritten in frequency domain:

$$C_L(k) = \pi\left[k^2 - 2jkC(k)\right]\frac{h(k)}{c} + \pi\left[k^2 a - jk + 2\left(1 - jk\left(\frac{1}{2} - a\right)\right)C(k)\right]\alpha(k) \tag{2.51a}$$

$$C_M(k) = \pi\left[k^2\frac{a}{2} - jk\left(\frac{1}{2} + a\right)C(k)\right]\frac{h(k)}{c} + \pi\left[\frac{1}{2}\left(-jk\left(\frac{1}{2} - a\right) + k^2 + \left(\frac{1}{8} + a^2\right)\right) + \left(\frac{1}{2} + a\right)\left(1 + jk\left(\frac{1}{2} - a\right)\right)C(k)\right]\alpha(k) \tag{2.51b}$$

Unsteady angle of attack and plunge motion are derived from the equation of the oscillatory motion:

$$x(A, \omega, t) = Ae^{-j\omega t} \tag{2.52}$$

The values of the amplitude A and ω are defined as functions of different parameters; the angular frequency is transformed to accept as input the reduced frequency as $\omega = \frac{kU_\infty}{b}$, while the oscillation amplitude is defined, for the pitch, as the value of the maximum angle of attack, $A = \alpha_{max}$, and for the plunge as percentage of the reference chord, $A = 10\%h_{max}$.

In Figures 2.12 and 2.13 the lift variation with different reduced frequencies is plotted. The reference velocity value is $U_\infty = 25m/s$ and the reference chord is $b = 0.5m$. $\alpha_{max} = 1°$ and $h_{max} = 10\%b$. The run-time is for $T = 2s$. Increasing the reduced frequency produces three effects:

- An increase in the number of cycles in given time. This is an effect of the increased angular frequency.
- An increase in the maximum produced lift for the plunging lift. This is due to an increased apparent angle of attack. Increasing the plunge velocity results in higher angle of attack, with resulting lift increase.
- A reduction in the maximum produced lift for the pitching airfoil. This is a result of the direct dependency of the lift from the pitching angular velocity, which in frequency domain is a function of ik.

Analyzing the effect on the plunging wing, the circulatory function adds an hysteresis on the generated lift, so that the lift dependency is not anymore linear. Being $C(k)$ multiplied by the reduced frequency ik(2.51a), the higher the frequency the the lower is the effect of the added circulation. When analyzing the pitching wing, where the hysteresis effect is damped by the circulatory function $C(k)$, but the maximum generated load is amplified by the circulation. Figure 2.16 reports the spectrum of the produced lift in frequency domain. As shown in Figure 2.16a, for the plunging wing, the reduced frequency increment produces a shift in the main wave component, which moves to higher frequencies and is amplified. In Figure 2.16b the lift production of a pitching wing can be seen, where the maximum amplitude is reduced due to an increase in circulatory effects. Observing the phase shift, while for small reduced frequencies the wave phase increases with the frequency, for $k = 0.5$ the phase is not subjected to major variations up to $16Hz$, where the phase drops significantly.

The Theodorsen model is widely applied in aeroelastic analysis, due to its simplicity and good approximation of loads generation ([22]). As shown in [24] a numerical implementation using the Vortice Lattice Method can be properly substituted by the Theodorsen theory.

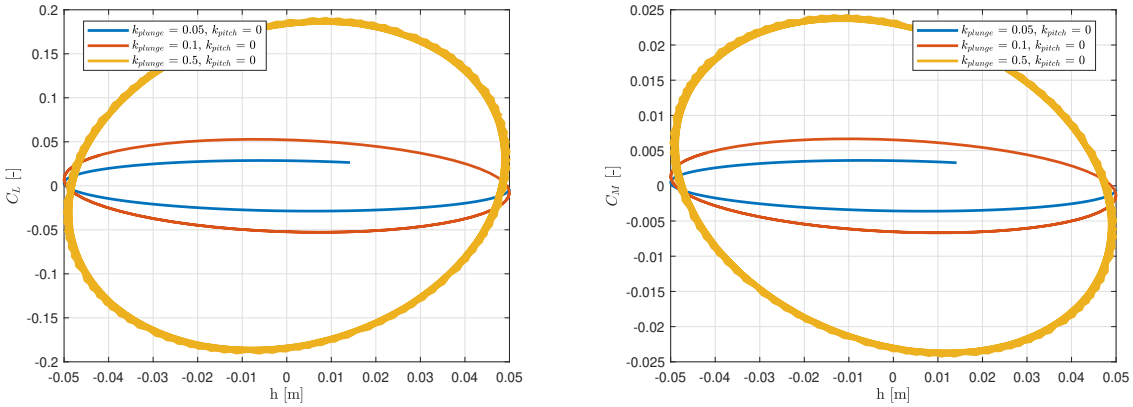

(a) Lift. (b) Moment.

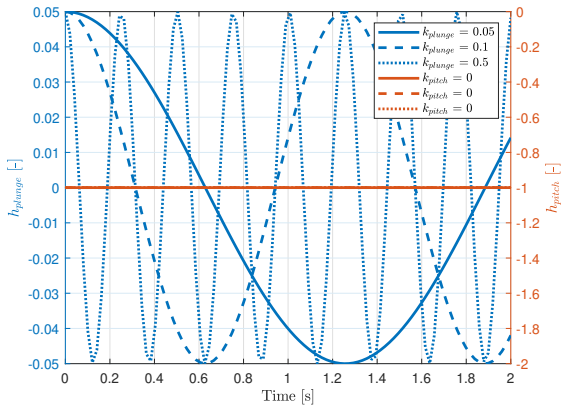

(c) Wing motion.

Figure 2.14: Plunging wing.

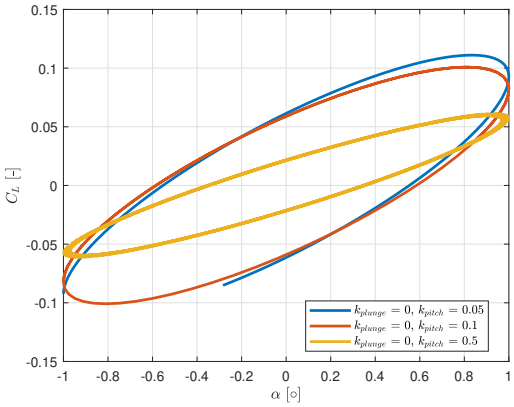

(a) Lift.

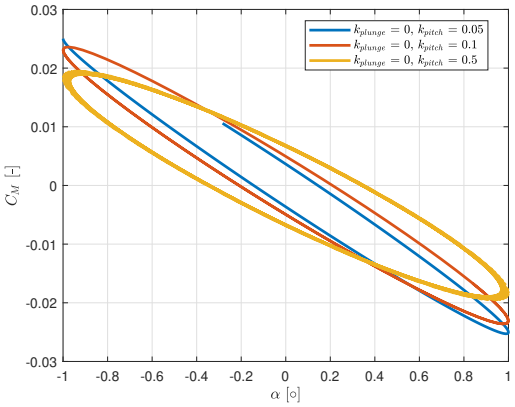

(b) Moment.

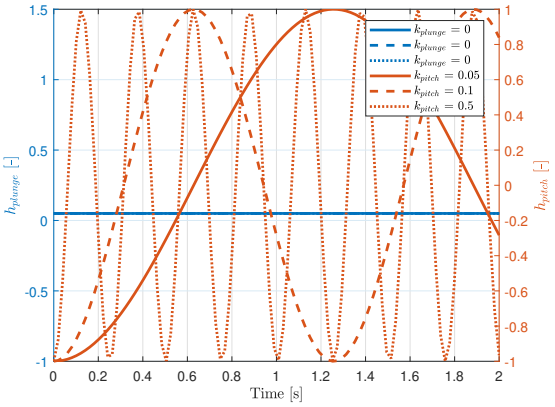

(c) Wing motion.

Figure 2.15: Pitching wing.

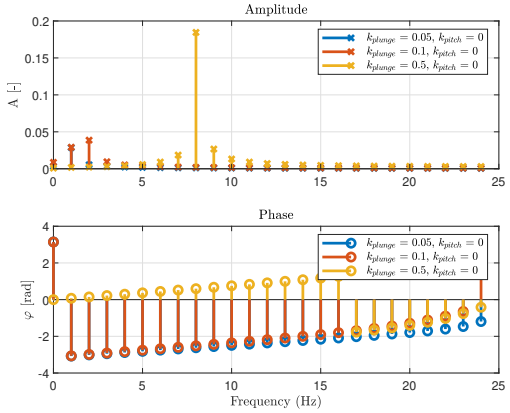

(a) Wing plunge, $h = 10\%$.

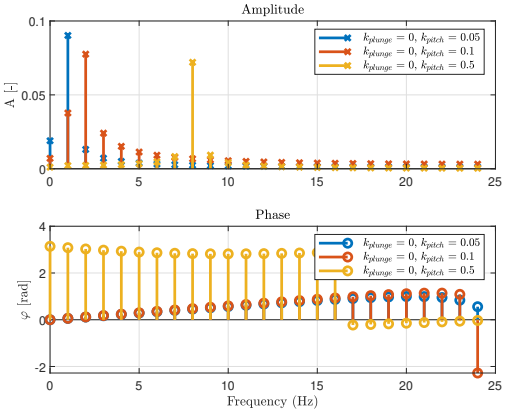

(b) Wing pitch, $\alpha = 1°$.

Figure 2.16: Frequency response.

3 | Validation of numerical solver

In this section a description of the developed code is given. A flowchart explains the aerodynamic and structural solver in separate sections. The validation cases are discussed to verify the code effectiveness for the following cases for the aerodynamic solver:

α	Solver	Wing	Motion	Red. Frequency k
var.	Steady	Infinite	None	0
var.	Unsteady	Infinite	None	0
cost.	Steady	Finite	None	0
cost.	Unsteady	Finite	None	0
cost.	Unsteady	Infinite	Plunge	0.05, 0.1, 0.5
var.	Unsteady	Infinite	Pitch	0.05, 0.1, 0.5

Table 3.1: Test cases for aerodynamic solver

The first two solution are compared to the solution obtained using X-FOIL ([1]). The Reynolds number convergence is ran to validate and exploiting the dependence of the produced loads with the considered flow velocity. The last two validation cases are compared to the Theodorsen ([3]) plunge and pitching cases at different reduced frequencies. The last case is ran correcting the Theodorsen lift coefficient with the finite wing C_{L_α}, to compare the computed lift with the analytical function. The validation cases for the structural solvers are in forms of modal shapes frequencies convergence w.r.t. number of elements. Those validations cases are not reported in this paper not being relevant in the context of this study.

3.1. Solvers description

The code is composed of 3 separate solvers, which can be ran stand alone or in conjunction one with the other. Only the aerodynamic solver will be described.
The input body is defined using a .json file, containing the following parameters:

The following flow chart describes the aerodynamics solver structure:

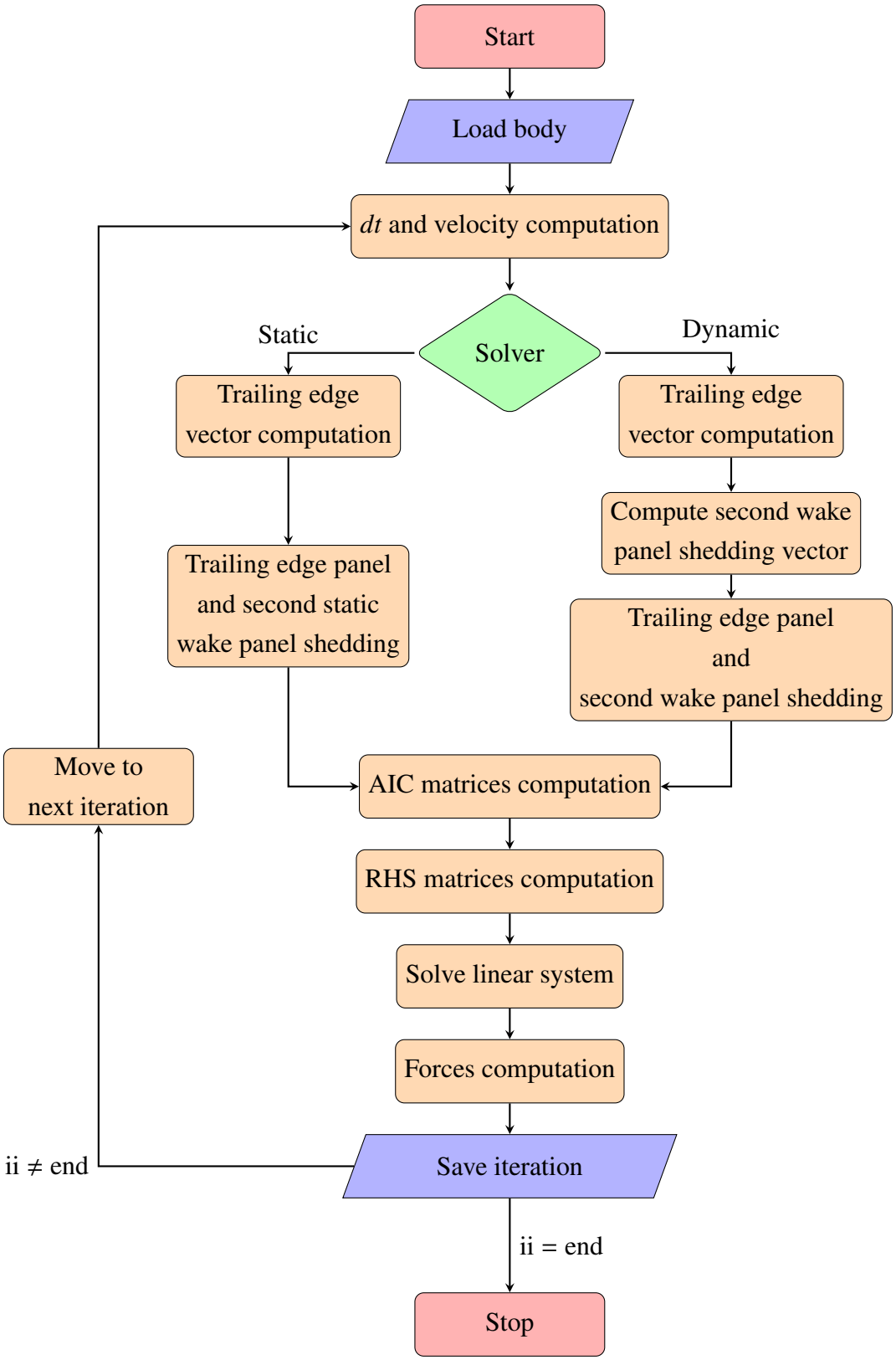

Figure 3.1: Aerodynamic solver flowchart

3.2. Validation cases

Three wings were tested to validate the code:

Span [m]	Chord [m]	Sweep [deg]	Dihedral [deg]	λ [$-$]	Root foil [m]	Tip foil [m]
500	0.5	0	0	1000	NACA0006	NACA0006
500	0.5	0	0	1000	NACA0020	NACA0020
5	0.5	0	0	10	NACA0020	NACA0020

Table 3.2: Validation wings

The first two wings are used to compare the compiled code with the data obtained using XFOIL [1]. The first wing $NACA-0006$ is chosen to have a thin airfoil, which can be compared to the classical thin airfoil theory [17]. The former $NACA-0020$ wings is analyzed to verify the effect of airfoil thickness on the C_{L_α}, while the latter is analyzed to verify the 3D effects on the wing performance.

3.2.1. Mesh independence

The first test conducted was a mesh convergence on the lift coefficient and the pressure distribution C_p, changing both the number of chord points and spanwise sections. The C_L sensitivity plot is shown in this section, while the C_p plots are reported in Appendix 6. For the following cases the solution used as reference is the 2D case, computed using XFOIL. This is to assess the convergence of the developed solver in respect to the ideal inviscid case. The theoretical result, computed using the equation $C_L = 2\pi\alpha$, is not used due to airfoil thickness.

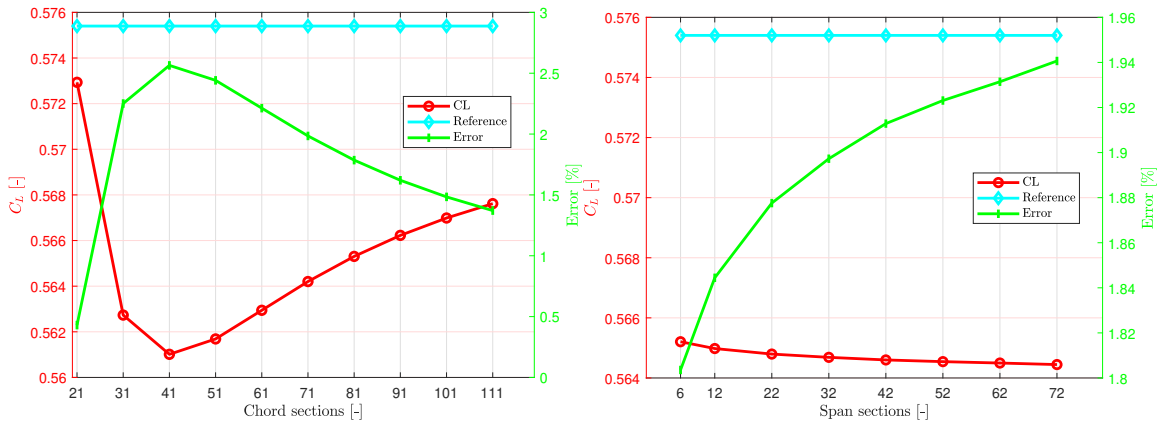

(a) Chord independence.

(b) Span independence.

Figure 3.2: NACA0006, $\lambda = 1000$, c=0.5 [m]

Looking at the trends figures 3.2a and 3.2b the major factor contributing to the convergence of the lift coefficient is the number of panels along the wing chord, reaching convergence for a value equal or greater to 71 chord panels. This is due to convergence of the C_p curves on the profile, as reported in 6. This has two major contributions: i) lift absolute value ii) Center Of Pressure (C.O.P) position, which has a direct influence on the generated pitching moment of the wing. Comparing Figures 3.3a and 3.3b, increasing the number of chord panels smooths the reach of the peak C_p value and reaching the stagnation point at the trailing edge. Compared to the 2D solution, the minimum C_p value reaches a smaller value, which could be explained by a minor interaction between bottom and top wing surfaces.

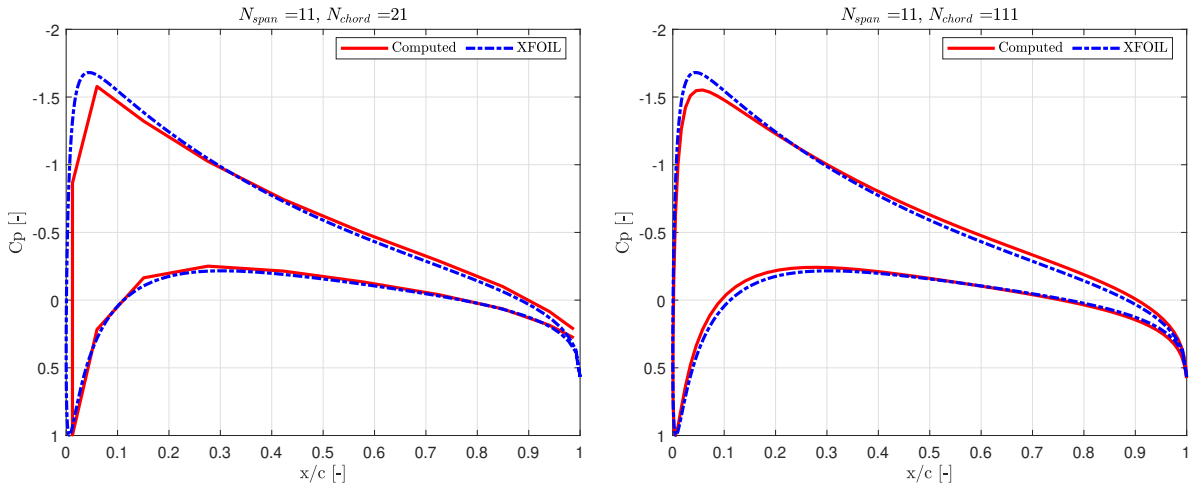

(a) C_p distribution, 21 chord panels.

(b) C_p distribution, 111 chord panels.

Figure 3.3: NACA-0020, λ = 1000, c=0.5 [m], C_p distribution

Span Sections [-]	Chord Sections [-]	C_L [-]	C_D [-]	C_M [-]	Time [s]
12	21	0.5706	0.0505	-0.0031	10.858
12	31	0.5601	0.0539	-0.0033	0.9644
12	41	0.5584	0.0533	-0.0034	1.4994
12	51	0.5592	0.0519	-0.0034	2.1301
12	61	0.5606	0.0506	-0.0035	2.9733
12	71	0.5619	0.0495	-0.0035	3.9394
12	81	0.5631	0.0487	-0.0035	4.9720
12	91	0.5641	0.0481	-0.0035	6.2746
12	101	0.5649	0.0476	-0.0035	7.6738
12	111	0.5655	0.0473	-0.0036	9.2589

Table 3.3: Mesh independence for number of panels chord, NACA-0006, λ = 1000

Span Sections [-]	Chord Sections [-]	C_L [-]	C_D [-]	C_M [-]	Time [s]
6	101	0.5651	0.0477	-0.0395	8.9674
12	101	0.5649	0.0476	-0.0395	13.425
22	101	0.5647	0.0476	-0.0395	31.103
32	101	0.5646	0.0476	-0.0395	74.193
42	101	0.5645	0.0476	-0.0395	123.95
52	101	0.5644	0.0476	-0.0395	200.85
62	101	0.5644	0.0476	-0.0395	354.57
72	101	0.5643	0.0476	-0.0395	460.71

Table 3.4: Mesh independence for span sections, NACA-0006, $\lambda = 1000$

Having reported the convergence analysis for the 0006 profile, the number of chosen panels is 81 chordwise and 10 spanwise. The aforementioned analysis is ran for the last two wings reported in 3.2, and the results are reported in the following tables.

Span Sections [-]	Chord Sections [-]	C_L [-]	C_D [-]	C_M [-]	Time [s]
12	21	0.5860	0.0462	-0.0496	1.2214
12	31	0.5923	0.0427	-0.0508	0.98179
12	41	0.5976	0.0418	-0.0516	1.4572
12	51	0.6012	0.0414	-0.0521	2.2074
12	61	0.6037	0.0412	-0.0525	2.9229
12	71	0.6056	0.0411	-0.0528	4.0395
12	81	0.6070	0.0411	-0.0531	5.2706
12	91	0.6082	0.0411	-0.0533	6.4457
12	101	0.6091	0.0411	-0.0534	7.9167
12	111	0.6098	0.0411	-0.0535	9.7516

Table 3.5: Mesh independence for number of panels chord, NACA-0020, $\lambda = 1000$

Span Sections [-]	Chord Sections [-]	C_L [-]	C_D [-]	C_M [-]	Time [s]
6	101	0.6094	0.0411	-0.0534	2.6297
12	101	0.6091	0.0411	-0.0534	9.0741
22	101	0.6089	0.0410	-0.0534	34.11
32	101	0.6087	0.0410	-0.0534	69.554
42	101	0.6086	0.0410	-0.0534	125.72
52	101	0.6086	0.0410	-0.0534	199.33
62	101	0.6085	0.0410	-0.0534	301.1
72	101	0.6084	0.0410	-0.0534	444.32

Table 3.6: Mesh independence for span sections, NACA-0020, $\lambda = 1000$

Span Sections [-]	Chord Sections [-]	C_L [-]	C_D [-]	C_M [-]	Time [s]
12	21	0.4603	0.0289	-0.0393	1.3256
12	31	0.4638	0.0261	-0.0403	1.1223
12	41	0.4674	0.0254	-0.0409	1.628
12	51	0.4699	0.0251	-0.0414	2.3674
12	61	0.4717	0.0249	-0.0417	3.088
12	71	0.4730	0.0248	-0.0419	3.9854
12	81	0.4741	0.0248	-0.0421	5.4101
12	91	0.4749	0.0247	-0.0423	6.6963
12	101	0.4756	0.0247	-0.0424	8.1336
12	111	0.4761	0.0247	-0.0425	9.7621

Table 3.7: Mesh independence for number of panels chord, NACA-0020, $\lambda = 10$

Span Sections [-]	Chord Sections [-]	C_L [-]	C_D [-]	C_M [-]	Time [s]
6	101	0.4945	0.0263	-0.0442	2.6825
12	101	0.4756	0.0247	-0.0424	8.4532
22	101	0.4661	0.0240	-0.0414	29.572
32	101	0.4628	0.0237	-0.0410	78.995
42	101	0.4612	0.0235	-0.0407	142.7
52	101	0.4602	0.0235	-0.0406	204.73
62	101	0.4596	0.0234	-0.0405	322.13
72	101	0.4592	0.0234	-0.0404	437.66

Table 3.8: Mesh independence for span sections, NACA-0020, $\lambda = 10$

Both chord panels and span panels trends confirms the results of the first analysis, further consolidating the choice of wing discretization.

3.2.2. $C_L - \alpha$ curve

A C_L vs α sweep is ran to evaluate the wing behaviour at different α. The first analysis is carried for a finite straight wing, sweeping from $\alpha = -10°$ to $\alpha = 10°$. The ran analysis is steady-state, to avoid the following effects:

- Dependence of the solution from the flow velocity, being the wake length fixed.
- Dependence of the solution from the pitching rate. The pitching rate is responsible for a variation in wake shape, which results in different influence coefficients computed and, hence, a different result.

As expected, the increased thickness produces a steeper curve compared to the theoretical $C_L = 2\pi$. Compared to the 2D solution obtained with X-FOIL, the higher thickness produces a reduction in lift at higher angle of incidence. This could be explained by a reduction in lift due to wing-tip vortices, despite the high wing AR. The peak error for each airfoil, compared to the 2D solution is the following:

Airfoil	$C_{L_{2D}}[-]$	$C_{L_{3D}}[-]$	C_L Error [%]	$C_{M_{2D}}[-]$	$C_{M_{3D}}[-]$	C_M Error [%]
0006	1.1465	1.1360	-0.9195	0.0058	0.0025	-57.1626
0020	1.2775	1.2102	-5.2710	0.0277	0.0224	-18.9815

Table 3.9: 2D vs 3D solution

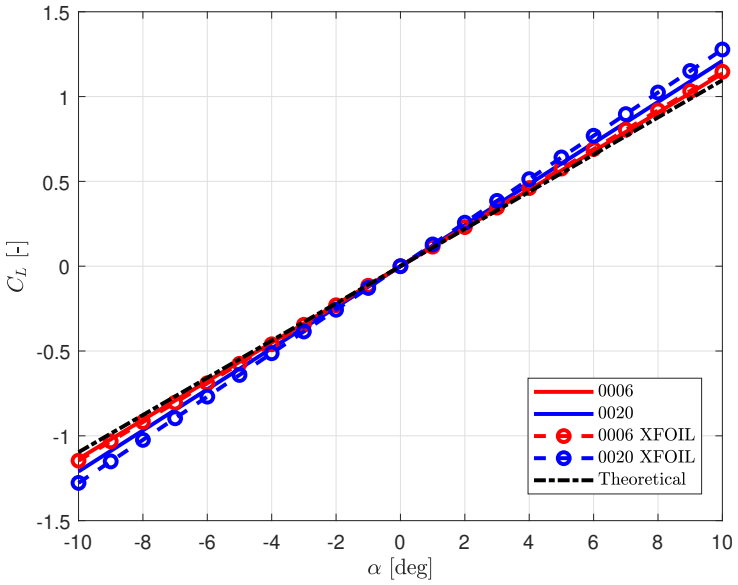

Figure 3.4: Solutions comparisons, $\lambda = 1000$, $\alpha - C_L$

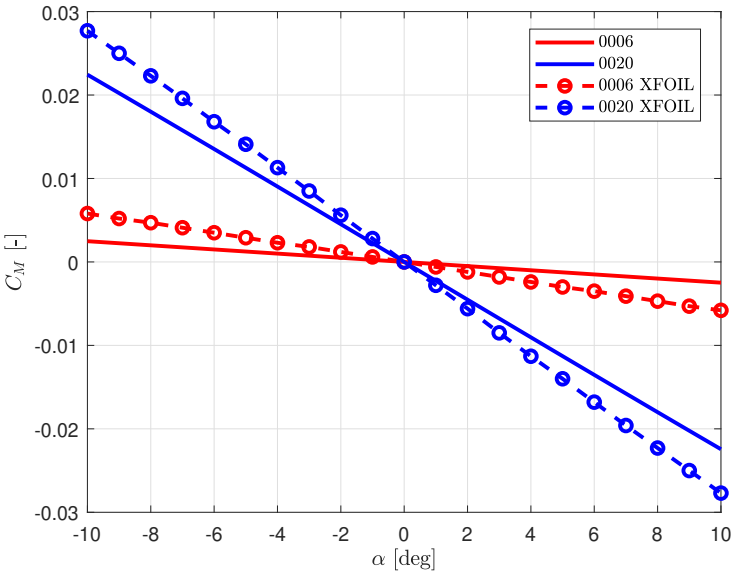

Figure 3.5: Solutions comparisons, $\lambda = 1000$, $\alpha - C_M$

3.2.3. Wake panel length dependency

A wake panel length dependency is carried over to evaluate the correlation between the generated lift and the flow condition. In Figure 3.6 the unsteady analysis is proposed. For the steady case the generated lift value is independent from the flow velocity, being the panel length fixed, and the computed lift is coincident for each flow condition. As expected for the steady case, being the wake completely developed, with the Kutta condition fully developed and unsteady effects not taken into consideration. The discrepancy in the generated C_L can be attributed to the body panel distance to the wake panels: this produces a difference in the computed influence coefficients, which effects the wake intensity and so on.

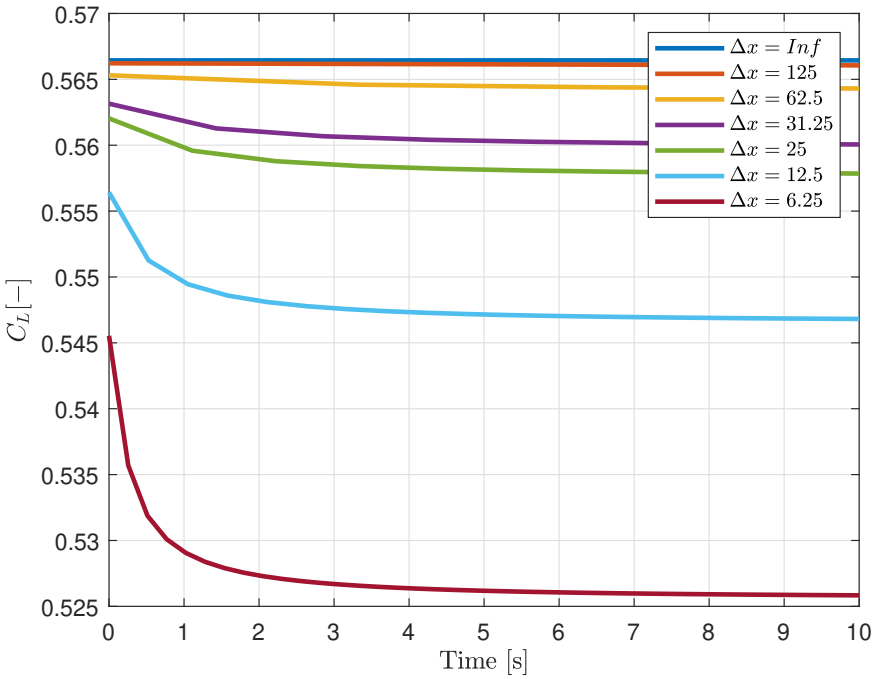

Figure 3.6: NACA0006, $\lambda = 1000$, $Time - C_L$, Unsteady

3.2.4. Pitch, plunge analysis

The Theodorsen model described in 2.2.6 is compared to the solution computed with the code written. Recalling the cases proposed in 3.1, the following cases were ran:

Motion	U	A	k	Time [s]	Steps
Plunge	25	10%	0.05, 0.1, 0.5	2	50
Pitch	25	1°	0.05, 0.1, 0.5	2	50

Table 3.10: Pitch and Plunge cases

The chosen flow velocity is $U_\infty = 25[m/s]$, with $\Delta t = 2/50 = 0.04[s]$.

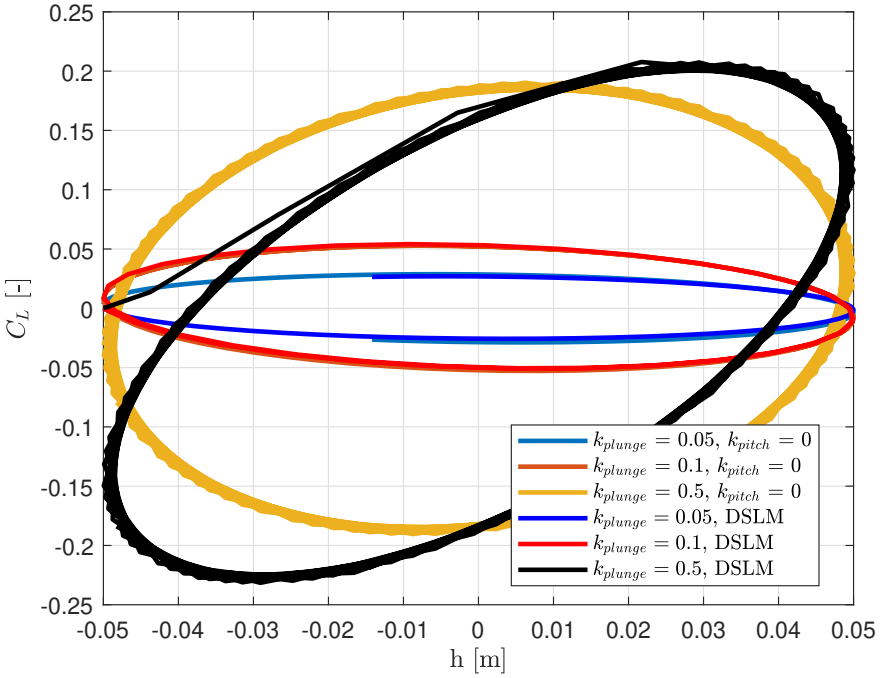

Figure 3.7: NACA0006, $\lambda = 1000$, h = 10%, plunge

The plot in Figute 3.7 shows that the C_L curve, when the sinusoidal motion is inverted, offsets from the Theodorsen model, which follows the ideal sinusoid. This effect is amplified when the reduced frequency is increased. This can be explained by the proximity of wake to the body. In the considered time frame, increasing the reduced frequency is responsible of more wake planes influencing the computed coefficients on the body.
Figure 3.9 shows an increase in lift production, with the maximum wave amplitude reached at the same frequency.

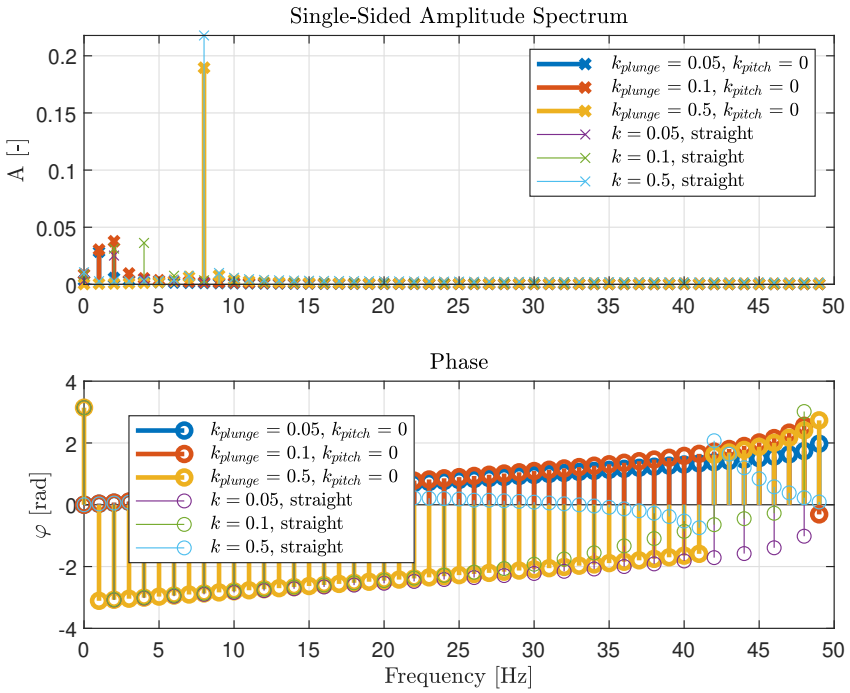

Figure 3.8: NACA0006, λ = 1000, h = 10%, plunge

Looking at Table 3.11 the reduced frequency has a direct influence on the phase lag, with the lag with reference to the Theodorsen case increasing with the increase of reduced frequency.

k	A_{DSLM}/A_{TH} [-]	$\Delta\varphi$[◦]
0.05	0.8834	-8.465
0.1	0.9610	-17.83
0.5	1.149	-26.00

Table 3.11: Plunge, h/c = 10%

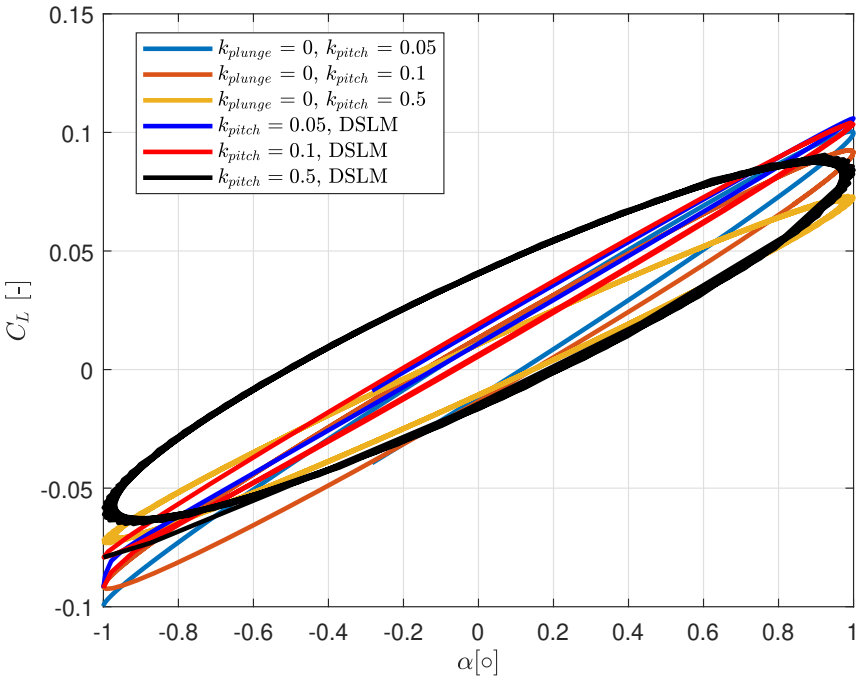

Figure 3.9: NACA0006, $\lambda = 1000$, $\alpha = 1°$, pitch

k	A_{DSLM}/A_{TH} [-]	$\Delta\varphi[\circ]$
0.05	0.9634	-6.5971
0.1	1.0391	-6.1037
0.5	1.0636	-13.2291

Table 3.12: Pitch, $\alpha = 1°$, phase differences

For the pitching case the difference between the different reduced frequencies is described by two different phenomena:

- Phase lag: as with the plunging case, the increase in reduced frequency produces an increase in the phase-lag between the ideal and computed solutions.
- Amplitude increase: the increase in reduced frequency produces an increase in the wave amplitude. For small reduced frequencies, a shift in the wave amplitude is achieved. The $k = 0.05$ frequency results in a $1Hz$ wave shift, $k = 0.1$ frequency results in a $2Hz$ wave shift while the $k = 0.5$ results in phase with the ideal case.

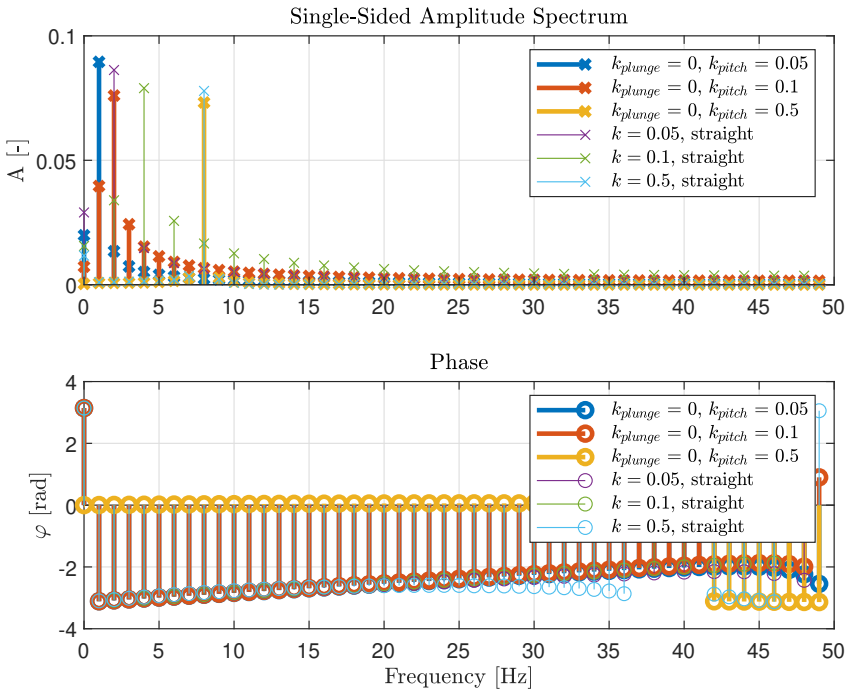

Figure 3.10: NACA0006, $\lambda = 1000$, $\alpha = 1°$, pitch

4 | Tubercles assessment

This chapter will be dedicated to combining all the methodologies developed and described in the previous chapters. The suction-side vortices are modelled using a vortex line progressively departing from the wing surface. The analysis of the wings with tubercles is carried by comparing 2 pairs of solutions:

- Linear L.E. - Wavy L.E.: the linear wing is compared to the wavy wing.
- Wavy L.E. with free-vortex - Wavy L.E. without free-vortex: the wavy wing solution is compared with the free vortex modelled and the free vortex not modelled.

In the first paragraph an evaluation of the vortices will be given, with a description of the surface induced velocities. A comparison with the reference experimental case will be described, evidencing the differences between the proposed model and the experiment results. In the last paragraph, harmonic pitching and plunging airfoils will be analyzed to assess the difference between the baseline geometry and the modified one.

4.1. Wavy leading edge and free-vortex evaluation

The chosen wing analyzed has the following properties:

Type	Root Profile	Tip Profile	Chord	λ	$A[\%]$	$f[\#]$
Linear	0020	0020	0.5	5	0	0
cos	0020	0020	0.5	5	0.15	6

Table 4.1: Study wing

where A is the tubercle amplitude referred to the wing reference chord and f is the number of valleys on the wing. The analysis for the finite wing is analogous to the one carried in Chapter 3, with both a plunging and pitching motion studied. The flow conditions and angle of incidence are $U_\infty = 25\ [m/s]$, and $\alpha = 5°$.

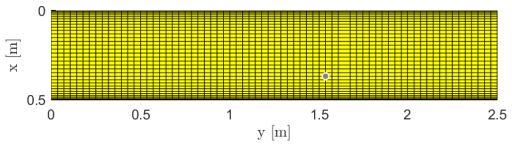

(a) Straight wing

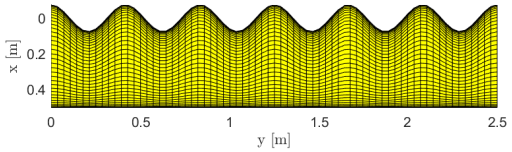

(b) Wavy wing

Figure 4.1: Wings geometries, top view

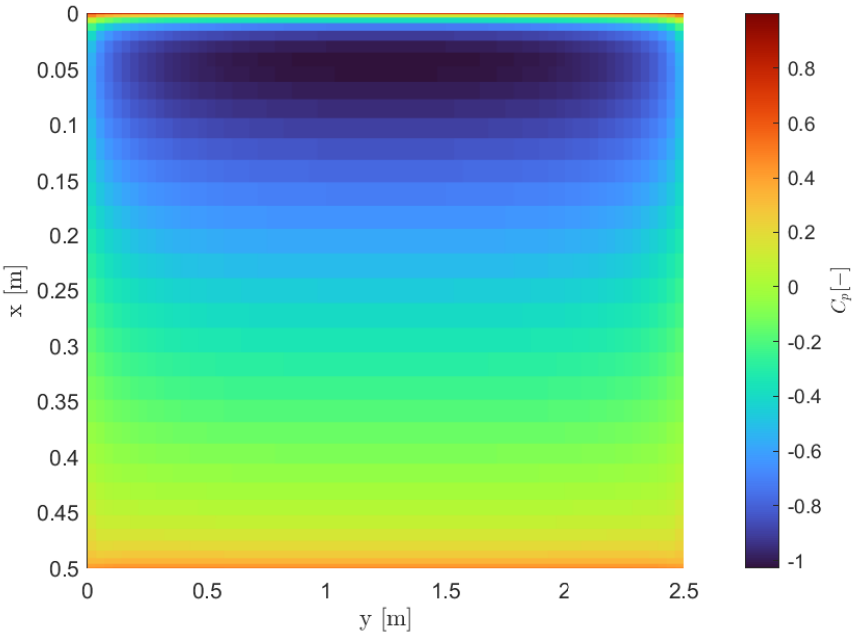

(a) Straight wing

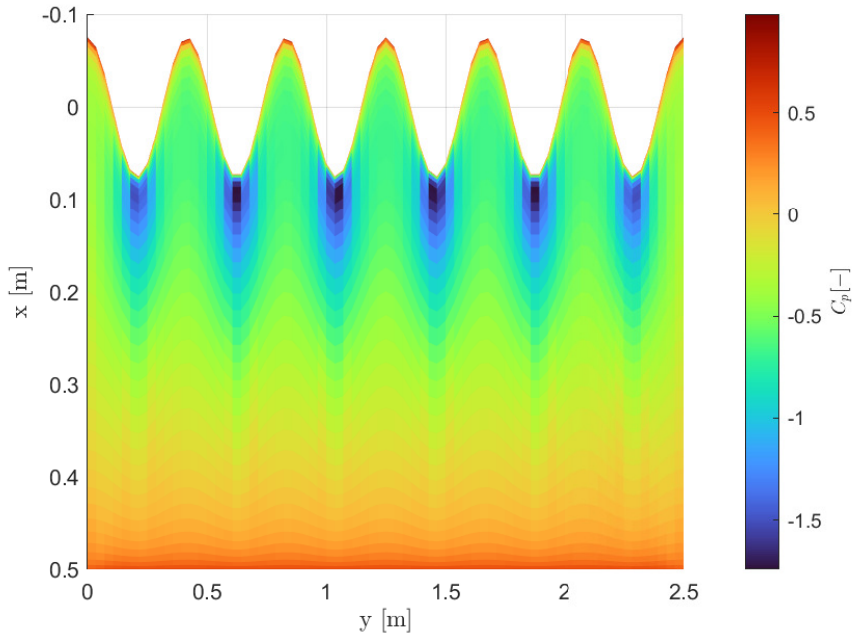

(b) Wavy wing

Figure 4.2: 3D C_p distribution, top view

In Figure 4.2 the effect of the tubercles becomes evident. The discontinuity on the leading edge produces a cross flow between profile peaks and valleys, which has the effect of reducing the average surface velocity in the principal flow direction x and the resulting C_p. In fact, the peak

velocity in the valleys is higher compared to the straight wing case, but the reduction which occurs in the sections between peaks and valleys produces a reduced overall C_L.
This reduction in the lift generated, however, can be attributed to the shape factor of the wing, being the free-vortices sources of induced velocities, which contributes to enhance the suction on the wing surface. Figure 4.4 proposes a comparison of the surface velocities of the straight and the wavy wing. The following considerations, for each velocity component, can be made:

- Chord-wise velocity, u: the peak surface velocity on the main axis reaches a higher value, by 7.6801%. This could be attributed to lower thickness and the presence of an inflow component, which results in higher velocity. No velocity contribution comes from the free-vortex, being the modelled axis parallel to the wing chord.
- Span-wise velocity, v: the velocity on the spanwise direction is massively boosted, by 178.1466%, due to the combined effect of the free vortices and the geometry itself, which favours a spanwise flow motion. Without the vortex modelling, the increase in induced flow velocity is 167.0713%, which exposes the geometrical dependency of this motion.
- Vertical velocity, w: the normal velocity is set to be 0 in the nominal case, not having traspiration velocity. As shown in Figure 4.4, this is not the case of the wavy wing, where the suction side vortices produces a vertical velocity component.

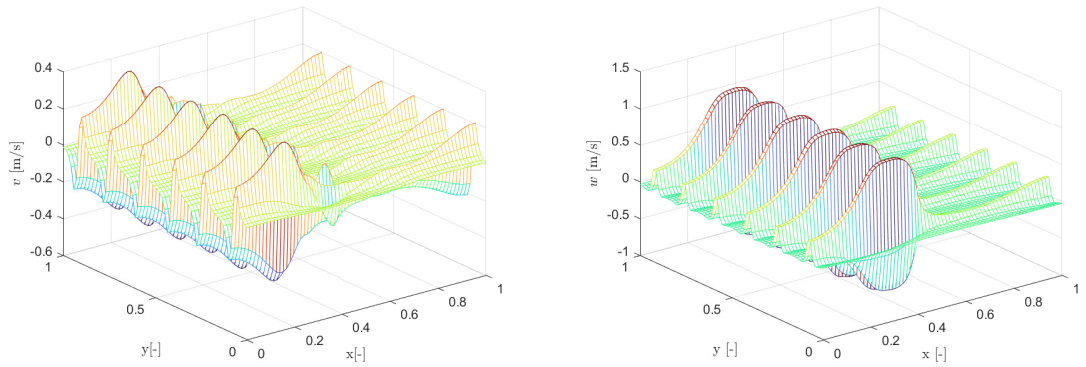

(a) v velocity component (b) v velocity component

Figure 4.3: Induced velocities on the wing

The plots in Figure 4.3 shows the induced velocity evolution along the wing chord, where the effect of the vortex core becomes evident, and the magnitude of the induced velocities, where the major component can be identified in the vertical one. The spanwise induced velocity accounts for the 13.6364% of the total spanwise velocity, while the normal induced velocity accounts for the entirety of the normal velocity.

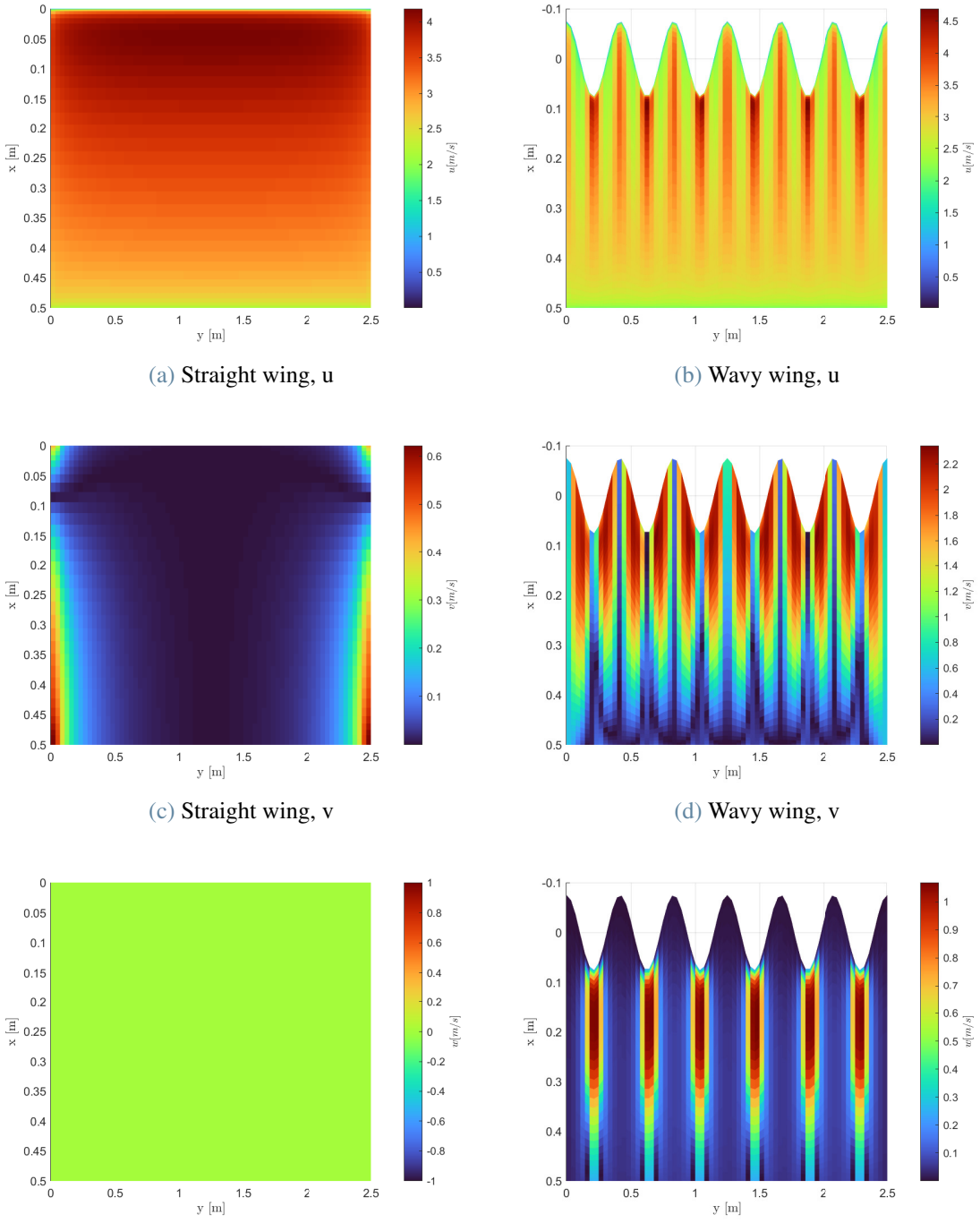

(a) Straight wing, u

(b) Wavy wing, u

(c) Straight wing, v

(d) Wavy wing, v

(e) Straight wing, w

(f) Wavy wing, w

Figure 4.4: Surface velocities, top view

The velocites direction is coherent with what was observed and described in Chapter 1. The two counter rotating vortices are exchanging velocity in the proximity of the surface, exchanging momentum in the boundary layer, delaying the separation.

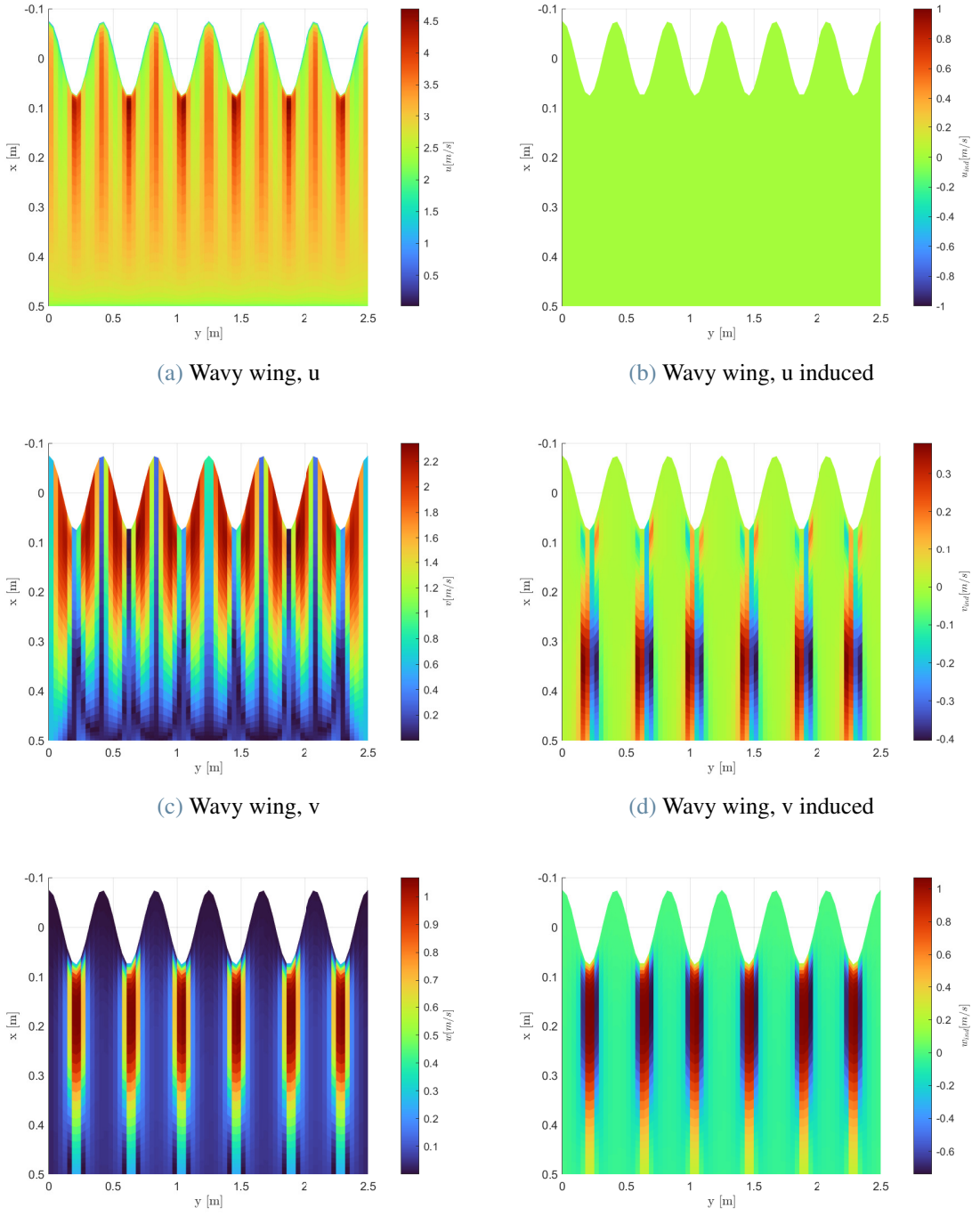

(a) Wavy wing, u

(b) Wavy wing, u induced

(c) Wavy wing, v

(d) Wavy wing, v induced

(e) Wavy wing, w

(f) Wavy wing, w induced

Figure 4.5: Surface velocities components, top view

A brief discussion on the results in Figure 4.6 is needed: in the top image the C_p maintains a low value even after the maximum peak. This contributes to a reduction in the pitching moment, having a more equilibrate load distribution. This will be further explored in Section 4.2

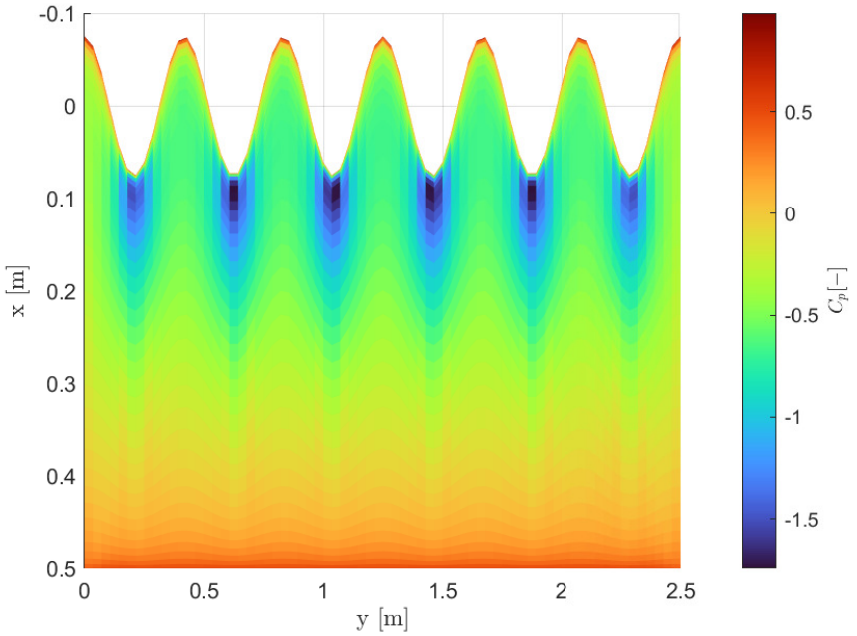

(a) Wavy wing, free vortex

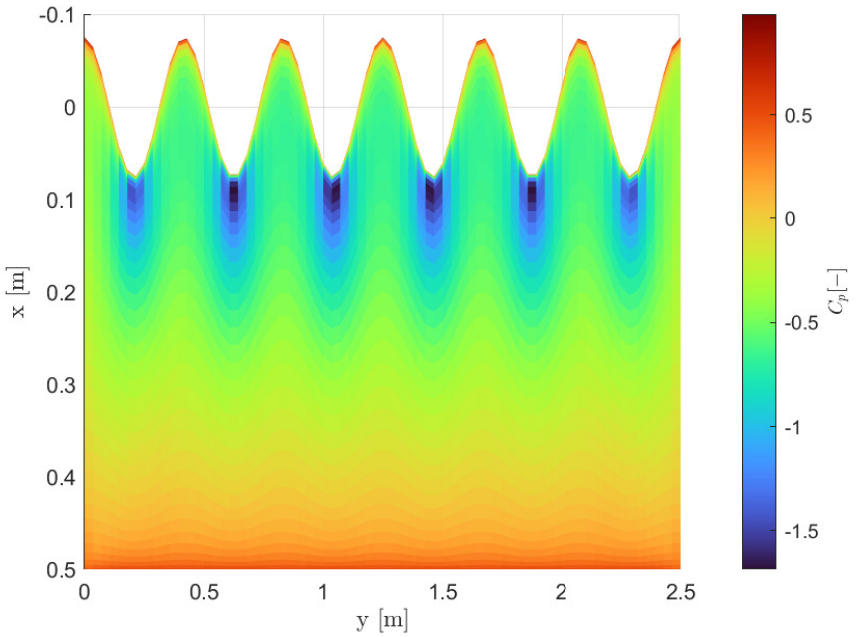

(b) Wavy wing, no free vortex

Figure 4.6: 3D C_p, free vortex comparison, top view

4.2. Hansen wing comparison

The chosen geometry to evaluate the leading edge vortices behavior is the wing proposed by Hansen *et al.* ([12]).

To conclude the analysis a comparison of different tubercles geometries will be analyzed, with different amplitudes and frequencies influencing the free-vortices distribution and intensity. The studied geometries will be the following:

$A/c[-]$	$\lambda/c[-]$	Label
0.06	0.21	A4λ15
0.06	0.43	A4λ30
0.06	0.86	A4λ60

Table 4.2: Geometries evaluated

The amplitude of the tubercles and the wavelength are defined as chord percentages. The experimental velocity was $U_\infty = 25[m/s]$ to achieve a $Re = 120000$. To achieve similar condition, the analysis will be run at the same velocity, in steady conditions. The steady condition is imposed by having a wake length of 10^3 to neglect wake geometrical influences. The wing consists of a $NACA - 0021$ profile, with chord length of 70 *mm* and span length of 459 *mm*. The baseline geometry, with straight leading edge, is compared with the geometries proposed in Table 4.2. The low Reynolds number was desirable to achieve a laminar boundary layer, which should benefit more from the leading edge vortices interacting with the boundary layer. Hansen ran the analysis on a 2D wing, with the wingtip bounded, and then proceeded to analyze the 3D wing case. The comparison between the 2D and 3D case is proposed in Figure 4.7. When reaching low angle of incidence, the 2D wing produces higher values of lift, as expected. The lift curve begins to display a nonlinear behaviour after $\alpha = 5°$. The author hypothesized the formation of a small separation bubble on the suction side, increasing the apparent camber-line and hence the lift generating capability. When reaching $\alpha = 12°$, the 2D baseline geometry abruptly stalls, whereas for the 3D case the stall, although still abrupt, is postponed to $\alpha = 14°$. Both the wavy wings, as expected, massively reduces the lift decrease, with the wing stall being more gentle and maintaining higher C_L values even at $\alpha = 20°$.

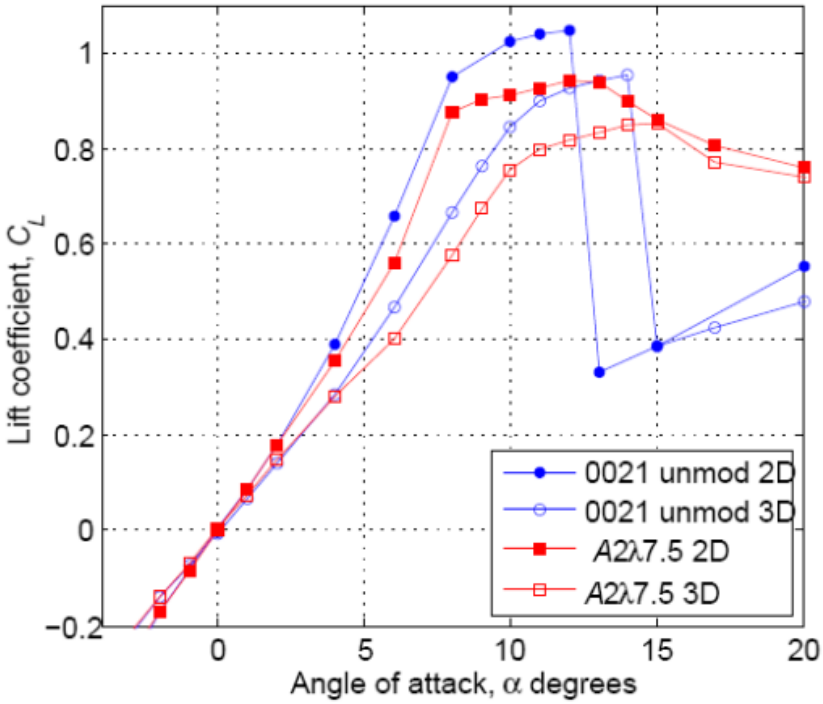

Figure 4.7: 2D vs 3D cases(from Hansen *et al.* [12])

The analyzed wings are proposed in Figure 4.8. As shown, the increase in tubercles amplitude makes the wing plan-form converge to the baseline geometry. The following panels distributions are used to discretize each wing:

- Chord: cosine distribution. N is the number of chord panels.

$$x = 0.5 + \cos\frac{(\pi - \pi * (0 : 1/N : 1))}{2} \tag{4.1}$$

- Span: even distribution. M is the number of span panels.

$$y = (0 : 1/M : 1) \tag{4.2}$$

The generated lift is taken into analysis. The expected curves should follow the experimental results up to higher angles of incidence, where the non-linearities should produce a deviation from the inviscid results. The lift reduction at higher incidences is not expected in the computed model, due to the absence of a boundary layer model.

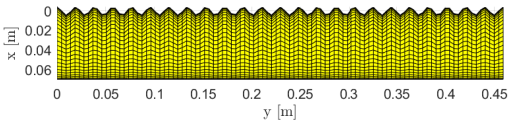

(a) $A/c = 0.06$, $\lambda/c = 0.21$

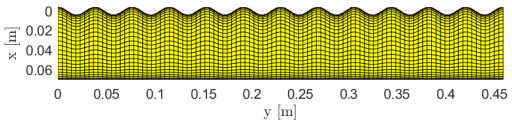

(b) $A/c = 0.06$, $\lambda/c = 0.43$

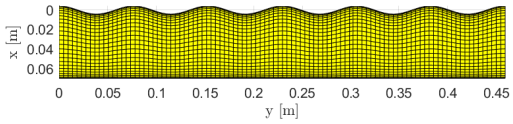

(c) $A/c = 0.06$, $\lambda/c = 0.86$

Figure 4.8: Evaluated geometries

The results are reported in Figures 4.9 and 4.10. Curves represented by circles are referring to the experimental data, while curves represented with crosses are referred to numerical data. As expected, when the experimental wings experience a reduction in produced lift due to the insurgence of stall, the developed model is not capable of replicating this effect. However, in the region $0 - 10°$, the model is fitting the experimental data. Compared to the test results the numerical model presents a more robust behaviour, with the curves having a more linear behaviour, albeit over predicting the actual lift coefficient. It's interesting to notice the abrupt stall of the $A4\lambda60$ configuration, which can be explained by the small amplitude variation between peaks and troughs. This makes the tubercle effect negligible, or even detrimental.

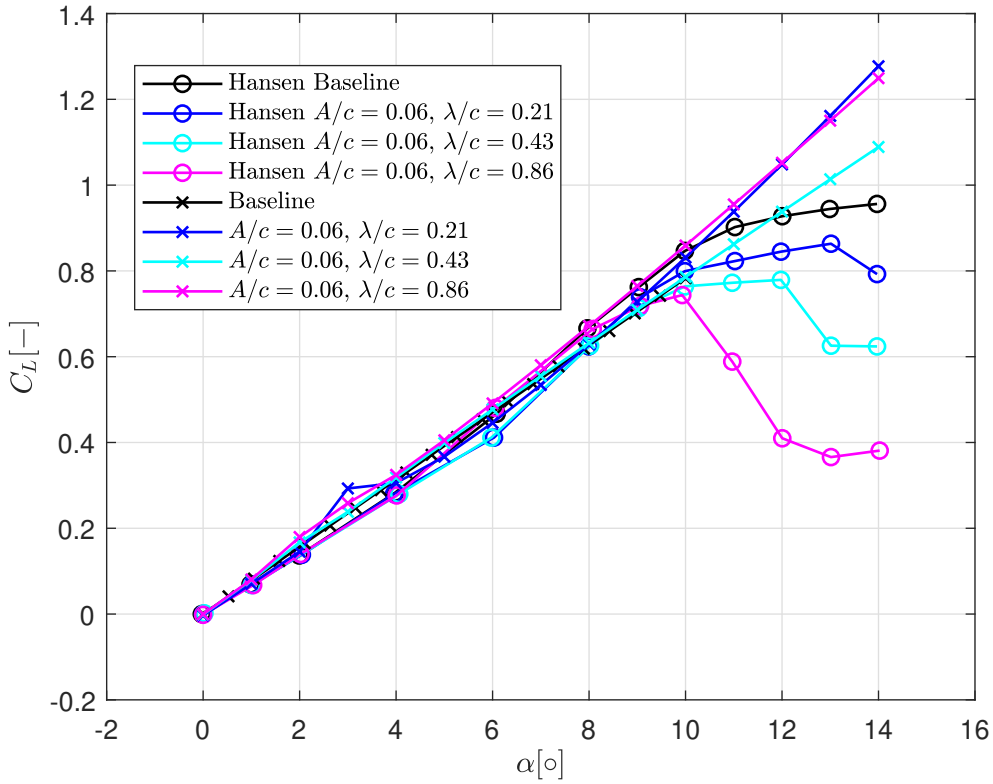

Figure 4.9: Computed lift versus experimental results

Looking at the curves at $\alpha = 5°$, the baseline and $A4\lambda60$ are more represented by the numerical model. The other geometries lift capabilities are over-predicted by the numerical model. It's interesting to notice that for the experimental results the difference in the generated lift is negligible between $A4\lambda15$ and $A4\lambda30$. For the $A4\lambda15$ the numerical model is closer to the experimental data.

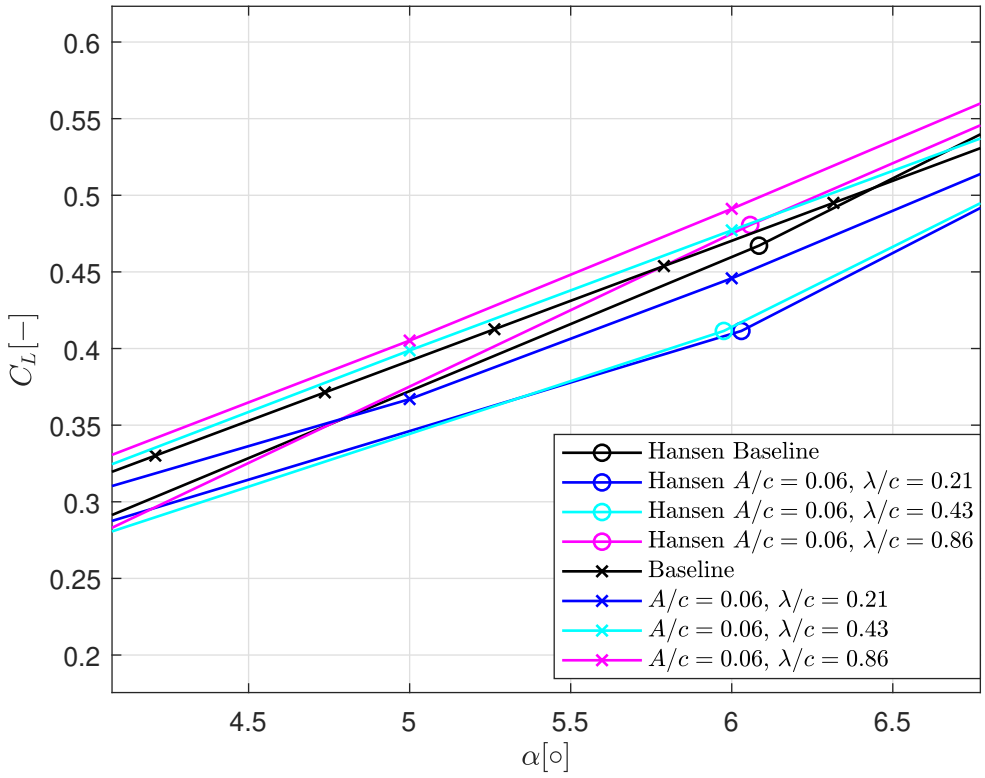

Figure 4.10: Lift curve detail at $\alpha = 5°$

When considering the polar at $\alpha = 10°$, the solution delta between the considered geometries is reduced, with all C_L values fitting in the range of $0.7 - 0.8$, as happening with the experimental data. The over-prediction of the numerical model is reduced with reference to the experimental solution. This could be explained by confirming the hypothesis of a separation bubble, which produces a non-linearity in the lift production. The overall comparison is deemed satisfactory, being the lift values consistent with the experimental results. The minor differences can be attributed to the viscous phenomenology happening in the experimental case. This is particularly evident when the wing is working at high angles of incidence, where important separations start to occur. However, when considering small amplitudes, the results can be described as coherent with the experimental evidence, hence the modelling base can be considered as a good estimation method for the potential modelling of tubercled wings.

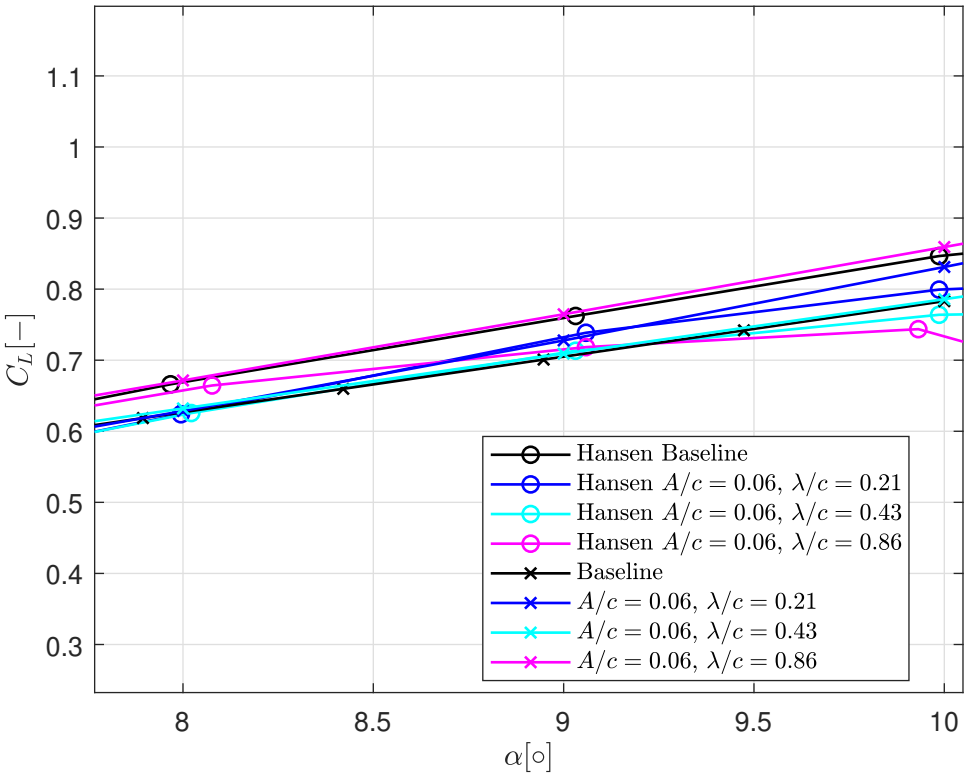

Figure 4.11: Lift curve detail at $\alpha = 10°$

4.3. Pitching and plunging motion

The analyzed motion is a pitching motion with amplitude $A = 1°$ and reduced frequency $k = 0.1$. The wings analyzed are the Hansen baseline geometry and the tubercled configuration $A4\lambda30$. In Figure 4.12 the response is reported.

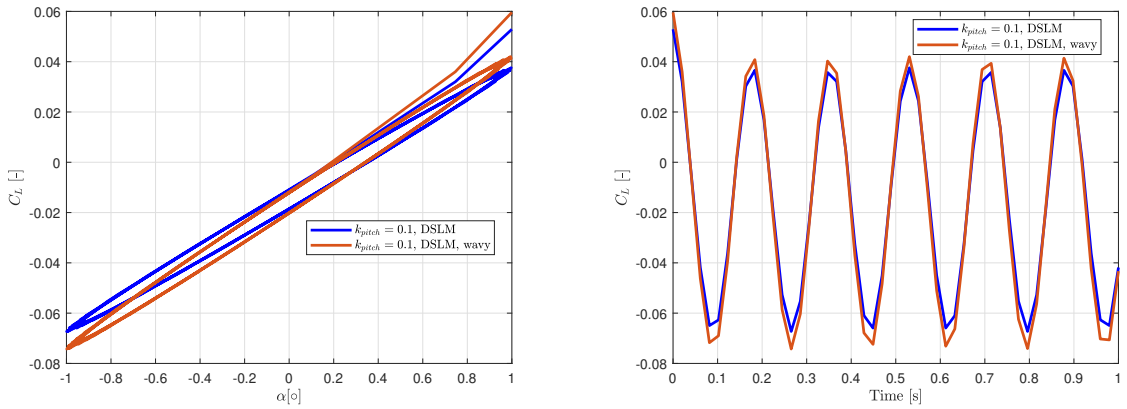

(a) $C_L - h$ curves.

(b) $C_L - T$ curves.

Figure 4.12: Pitching wing with modelled free vortex

The maximum lift production is increased. The phase lag between the baseline geometry and the tubercled geometry is negligible, both for the C_L and the C_M. When looking at Figure 4.13, the amplitude increase becomes more evident, with the maximum C_L increase occurring at $f = 12\ Hz$. The phase lag is increasing with the frequency for the base case, only to see a sudden drop at higher frequencies. For the tubercled geometry, the phase lag is constant for a wide frequency spectrum, and has a decrease when reaching frequencies above 30 Hz.

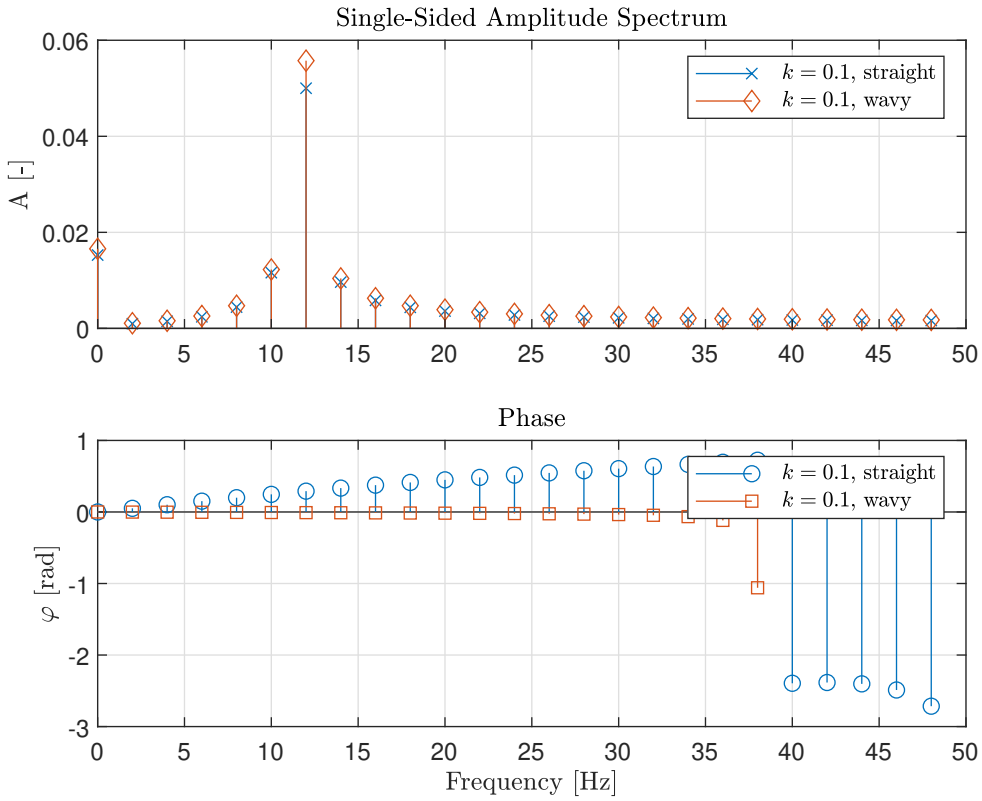

Figure 4.13: Pitching wing with modelled free vortex, frequency response

	k	$A_{wavy}/A_{straight}$ [-]	$\Delta\varphi[\circ]$
C_L	0.1	1.1146	1.5857
C_M	0.1	1.1516	1.4490

Table 4.3: Waves amplitude and phase Δs, pitch, $\alpha = 5°$

5 | Conclusions and future development

The introduction of tubercles and leading edge vortices provided the expected results. A decrease in C_L at low angles of incidence was observed, in accordance with literature. This can be attributed to the nonuniform shape of the leading edge, which resulted in cross flow phenomena across the wing surface, decreasing the overall suction and as such reducing the overall lift.
The modelling of the free vortices enabled the induction of surface spanwise and normal velocities, that coupled with the pressure distribution granted by the presence of peaks and troughs produces the increases in peak pressure.
The wing performance followed what was observed in precedent studies. A reduction in the tubercle amplitude and wavelength results in a pressure distribution and produced lift converging with the unmodified geometry. The results obtained shown the effect of the modelled tubercles and leading edge vortices, being the number of vortices a direct influence on the lift production. When the wing is subjected to a pitching harmonic motion, the maximum lift produced is increased, due to the effect of the induced velocity on the wing surface. The increase of 11% in lift production is accompanied by a slight phase lag. This effect demonstrates the solidity of the modelling choice, achieving what is observed in experimental studies. Future developments to increment the solution accuracy are mandatory, in order to use the vortex not for inducing higher surface velocities, but to use this induced velocity to delay flow separation. Future works to increase the potential application of the developed code are:

- Boundary layer modelling: a boundary layer modelling is required to describe flow separation, and analyze the effect of the vortices on the boundary layer momentum to delay separation.
- Dynamic vortex modelling: the detachment point of the vortex from the wing, along with the vortex core radius, should be flow dependent, instead of imposed in advance.
- Code redevelopment in different language: the requirement of a fine mesh to properly design the tubercles geometry produces big matrices, which results in long computational times. The usage of different programming language, along with a more efficient parallel computing, would ensure higher accuracy in geometrical description of the wing.

Bibliography

[1] Xfoil. https://web.mit.edu/drela/Public/web/xfoil/. Version: 6.99.

[2] J. Alba-Maestre, K. P. van Reine, T. Sinnige, and S. G. P. Castro. Preliminary propulsion and power system design of a tandem-wing long-range eVTOL aircraft. *Applied Sciences*, 11(23):11083, Nov. 2021. doi: 10.3390/app112311083. URL https://doi.org/10.3390/app112311083.

[3] S. L. Brunton and C. W. Rowley. Empirical state-space representations for theodorsen's lift model, Apr 2013. URL http://dx.doi.org/10.1016/j.jfluidstructs.2012.10.005.

[4] D. M. Bushnell and K. J. Moore. Drag reduction in nature. *Annual Review of Fluid Mechanics*, 23(1):65–79, 1991. doi: 10.1146/annurev.fl.23.010191.000433.

[5] F. R. Butt and T. Talha. Numerical investigation of the effect of leading-edge tubercles on propeller performance. *Journal of Aircraft*, 56(3):1014–1028, May 2019. doi: 10.2514/1.c034845. URL https://doi.org/10.2514/1.c034845.

[6] R. R. Colpitts, R. E. Perez, and P. W. Jansen. Effect of leading-edge tubercles on rotor blades. In *AIAA AVIATION 2020 FORUM*. American Institute of Aeronautics and Astronautics, June 2020. doi: 10.2514/6.2020-2763. URL https://doi.org/10.2514/6.2020-2763.

[7] R. R. Colpitts, R. E. Perez, and P. W. Jansen. Effect of leading-edge tubercles on rotor blades. *AIAA AVIATION 2020 FORUM*, Jun 2020. doi: 10.2514/6.2020-2763.

[8] B. F. N. Daniel T. H. New. *Flow Control Through Bio-inspired Leading-Edge Tubercles*. 5 edition, 2020.

[9] A. G. Domel, M. Saadat, J. C. Weaver, H. Haj-Hariri, K. Bertoldi, and G. V. Lauder. Shark skin-inspired designs that improve aerodynamic performance. *Journal of The Royal Society Interface*, 15(139):20170828, Feb. 2018. doi: 10.1098/rsif.2017.0828. URL https://doi.org/10.1098/rsif.2017.0828.

[10] J. Favier, A. Pinelli, and U. Piomelli. Control of the separated flow around an airfoil using

a wavy leading edge inspired by humpback whale flippers. *Comptes Rendus Mécanique*, 340(1–2):107–114, Jan 2012. doi: 10.1016/j.crme.2011.11.004. URL http://dx.doi.org/10.1016/j.crme.2011.11.004.

[11] L. A. Garrow, B. J. German, and C. E. Leonard. Urban air mobility: A comprehensive review and comparative analysis with autonomous and electric ground transportation for informing future research. *Transportation Research Part C: Emerging Technologies*, 132: 103377, Nov. 2021. doi: 10.1016/j.trc.2021.103377. URL https://doi.org/10.1016/j.trc.2021.103377.

[12] K. Hansen, R. Kelso, and B. Dally. An investigation of three-dimensional effects on the performance of tubercles at low reynolds numbers. 12 2010.

[13] J. Hess and A. Smith. Calculation of potential flow about arbitrary bodies. *Progress in Aerospace Sciences*, 8:1–138, 1967. ISSN 0376-0421. doi: https://doi.org/10.1016/0376-0421(67)90003-6.

[14] T. Hommes, J. Bosschers, and H. W. M. Hoeijmakers. Evaluation of the radial pressure distribution of vortex models and comparison with experimental data. *Journal of Physics: Conference Series*, 656:012182, Dec. 2015. doi: 10.1088/1742-6596/656/1/012182. URL https://doi.org/10.1088/1742-6596/656/1/012182.

[15] J. T. Hrynuk and D. G. Bohl. The effects of leading-edge tubercles on dynamic stall. *Journal of Fluid Mechanics*, 893, Apr. 2020. doi: 10.1017/jfm.2020.216. URL https://doi.org/10.1017/jfm.2020.216.

[16] A. P. Joseph Katz. *Low-Speed Aerodynamics*. 2 edition, 2010.

[17] J. D. A. Jr. *Fundamental of Aerodynamics*. 5 edition, 2011.

[18] H. Kim, J. Kim, and H. Choi. Flow structure modifications by leading-edge tubercles on a 3d wing. *Bioinspiration & Biomimetics*, 13(6):066011, Oct 2018. doi: 10.1088/1748-3190/aae6fc.

[19] J. W. Kim, S. Haeri, and P. F. Joseph. On the reduction of aerofoil–turbulence interaction noise associated with wavy leading edges, Mar 2016.

[20] D. Miklosovic, M. Murray, L. Howle, and F. Fish. Leading-edge tubercles delay stall on humpback whale (megaptera novaeangliae) flippers. *Physics of Fluids*, 16, 03 2004. doi: 10.1063/1.1688341.

[21] B. F. Ng, E. J. G. Ong, R. Palacios, and T. H. New. Effects of leading-edge tubercles on structural dynamics and aeroelasticity. In *Flow Control Through Bio-inspired Leading-*

Edge Tubercles, pages 147–173. Springer International Publishing, 2020. doi: 10.1007/978-3-030-23792-9_7. URL https://doi.org/10.1007/978-3-030-23792-9_7.

[22] S. Ōtomo, S. Henne, K. Mulleners, K. Ramesh, and I. M. Viola. Unsteady lift on a high-amplitude pitching aerofoil. *Experiments in Fluids*, 62(1), Dec. 2020. doi: 10.1007/s00348-020-03095-2. URL https://doi.org/10.1007/s00348-020-03095-2.

[23] F. P. Watts. The influence of passive, leading edge tubercles on wing performance. page 9, 2001.

[24] M. Parenteau and E. Laurendeau. A general modal frequency-domain vortex lattice method for aeroelastic analyses. *Journal of Fluids and Structures*, 99:103146, Nov. 2020. doi: 10.1016/j.jfluidstructs.2020.103146. URL https://doi.org/10.1016/j.jfluidstructs.2020.103146.

[25] N. Rostamzadeh, K. Hansen, and R. Kelso. Tubercled wing flow physics and performance. In *Flow Control Through Bio-inspired Leading-Edge Tubercles*, pages 41–68. Springer International Publishing, 2020. doi: 10.1007/978-3-030-23792-9_2. URL https://doi.org/10.1007/978-3-030-23792-9_2.

[26] A. Skillen, A. Revell, A. Pinelli, U. Piomelli, and J. Favier. Flow over a wing with leading-edge undulations. *AIAA Journal*, 53, 10 2014. doi: 10.2514/1.J053142.

[27] L. Wen, J. C. Weaver, P. J. M. Thornycroft, and G. V. Lauder. Hydrodynamic function of biomimetic shark skin: effect of denticle pattern and spacing. *Bioinspiration & Biomimetics*, 10(6):066010, Nov. 2015. doi: 10.1088/1748-3190/10/6/066010. URL https://doi.org/10.1088/1748-3190/10/6/066010.

6 | Appendix A

6.1. Convergence plots figures

6.1.1. NACA-0006

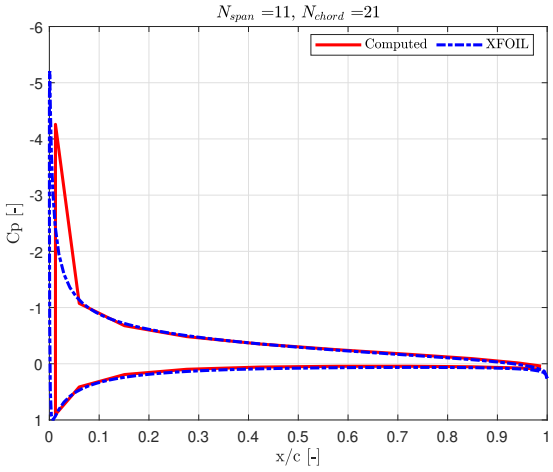

(a) 11 chord sections, 20 span sections

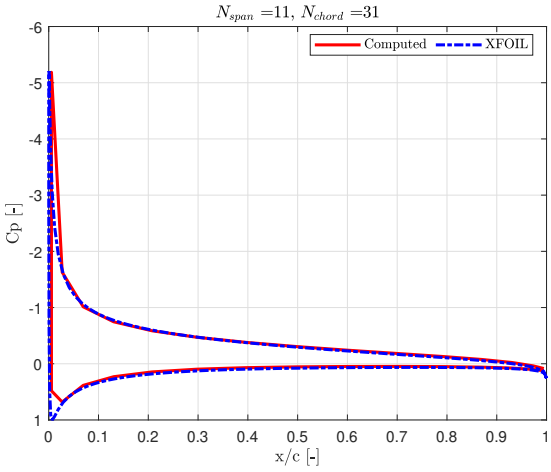

(b) 21 chord sections, 20 span sections

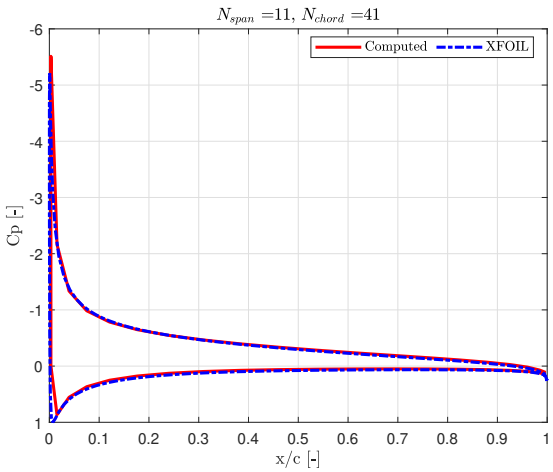

(c) 31 chord sections, 20 span sections

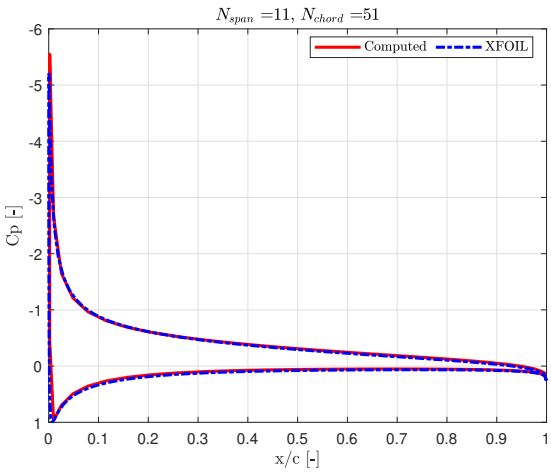

(d) 41 chord sections, 20 span sections

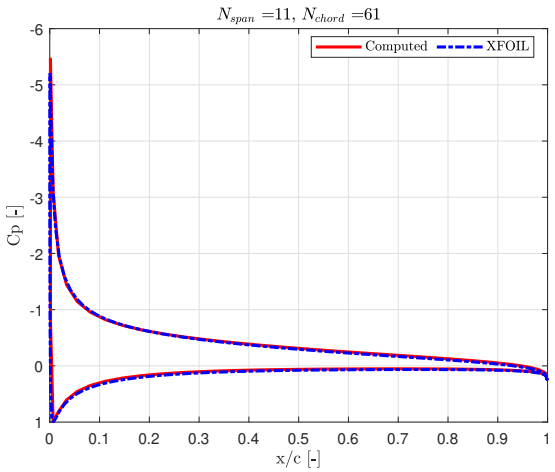

(e) 51 chord sections, 20 span sections

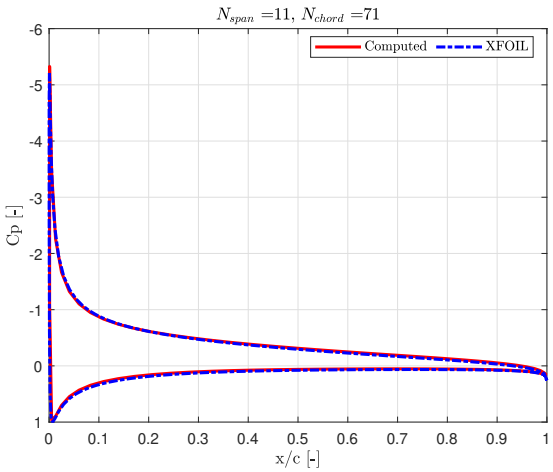

(f) 61 chord sections, 20 span sections

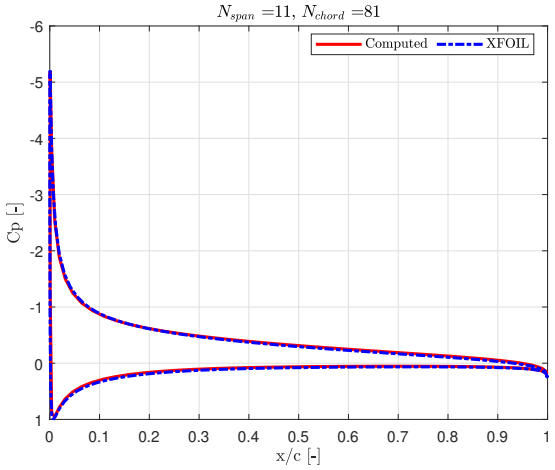

(g) 71 chord sections, 20 span sections

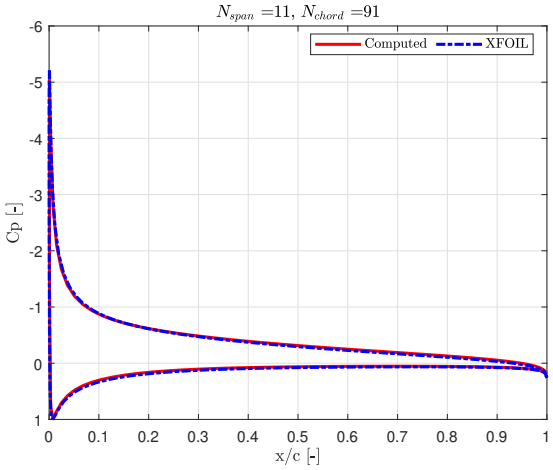

(h) 81 chord sections, 20 span sections

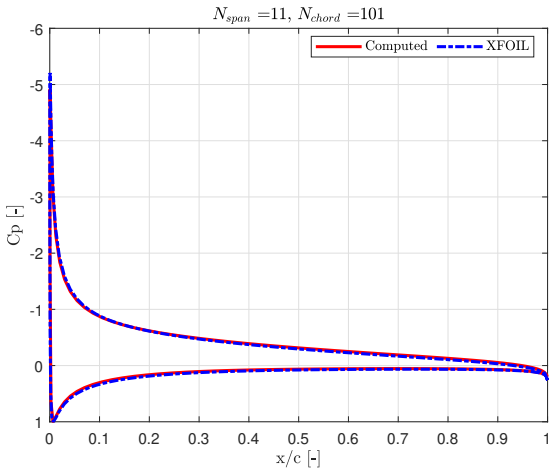

(i) 91 chord sections, 20 span sections

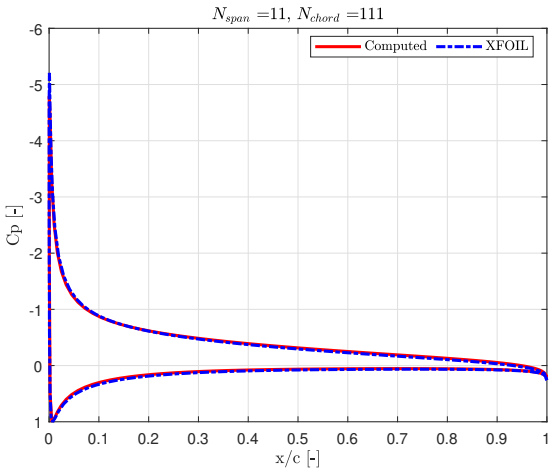

(j) 101 chord sections, 20 span sections

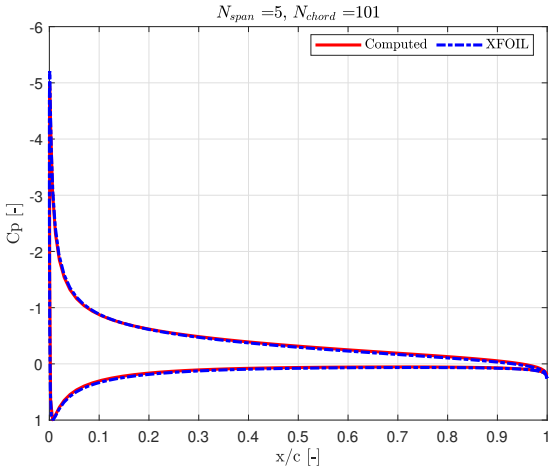

(k) 51 chord sections, 4 span sections

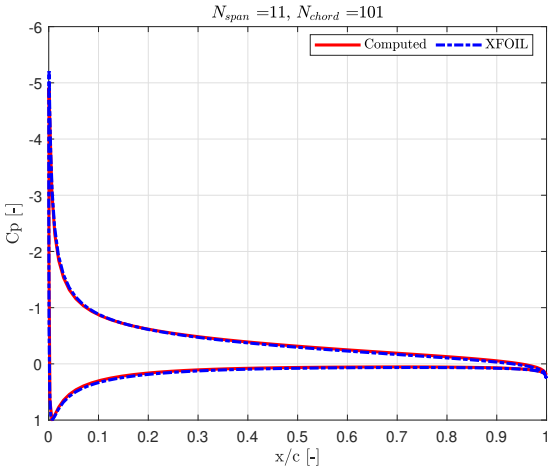

(l) 51 chord sections, 10 span sections

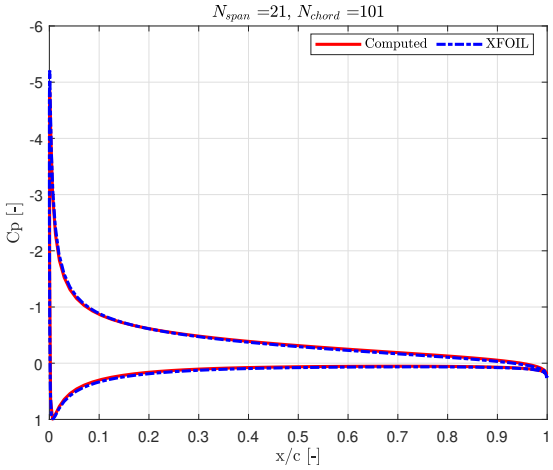

(m) 51 chord sections, 20 span sections

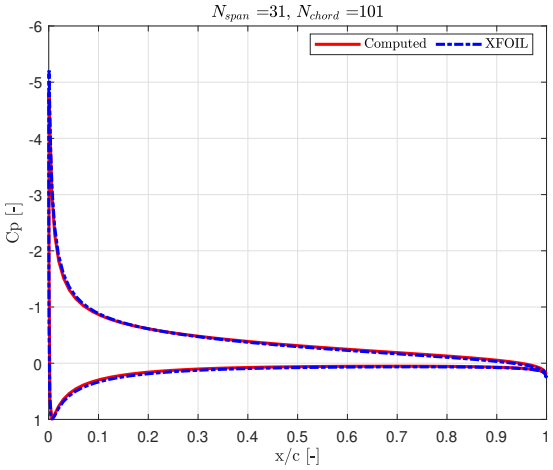

(n) 51 chord sections, 30 span sections

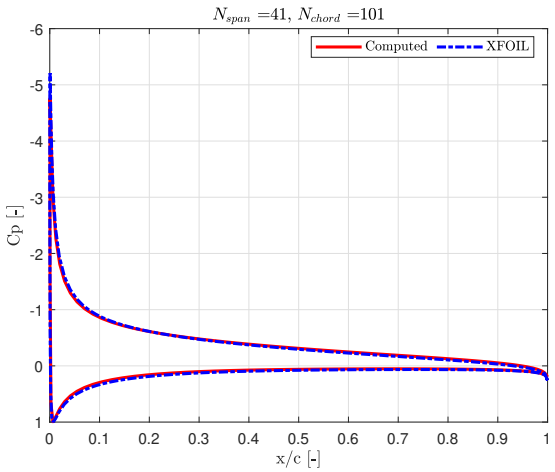

(o) 51 chord sections, 40 span sections

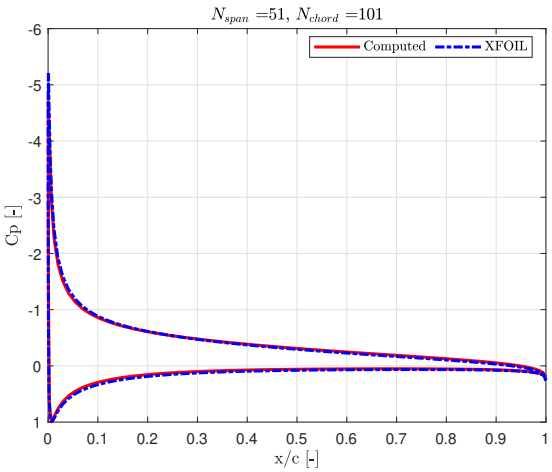

(p) 51 chord sections, 50 span sections

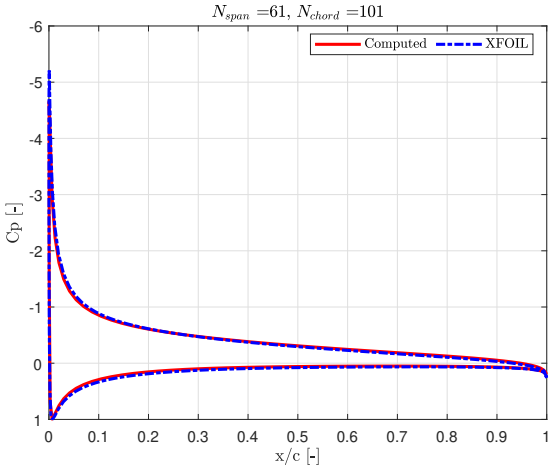

(q) 51 chord sections, 60 span sections

6.1.2. NACA-0020

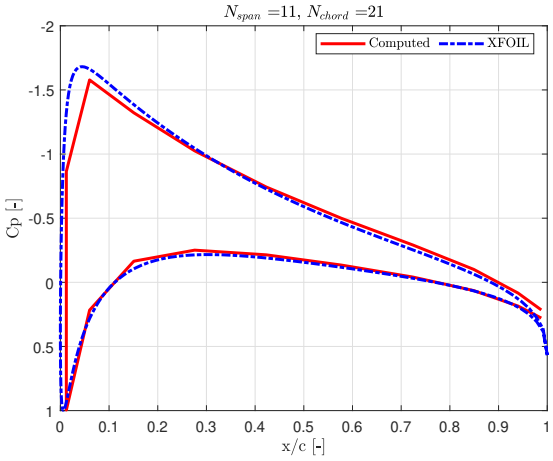

(a) 11 chord sections, 20 span sections

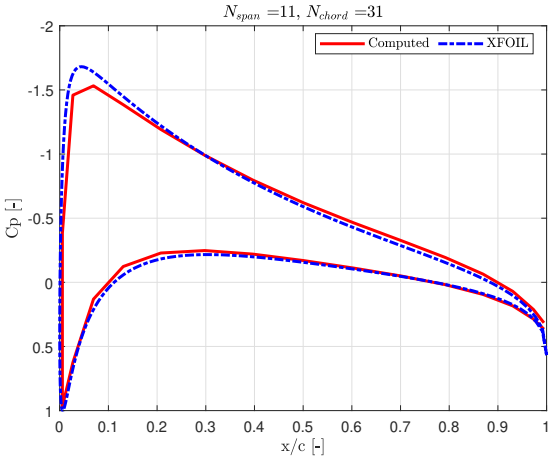

(b) 21 chord sections, 20 span sections

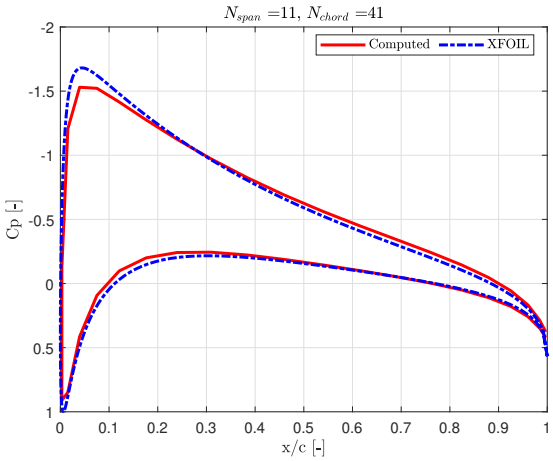

(c) 31 chord sections, 20 span sections

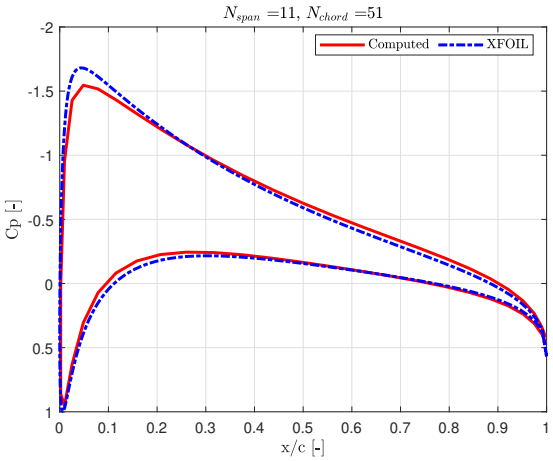

(d) 41 chord sections, 20 span sections

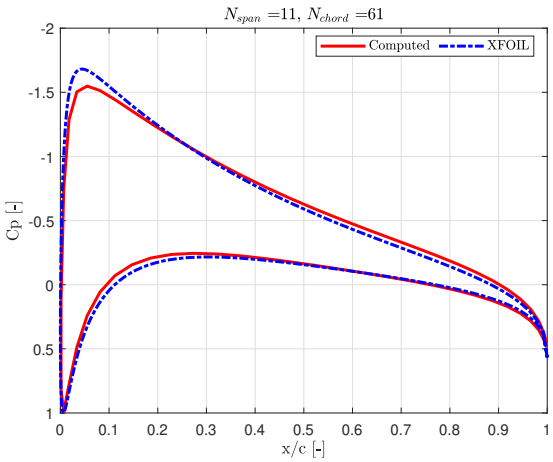

(e) 51 chord sections, 20 span sections

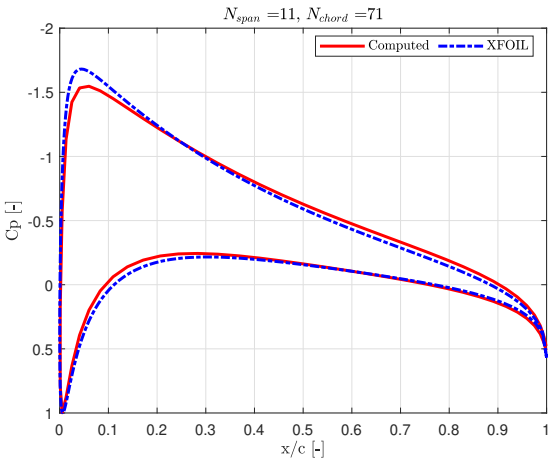

(f) 61 chord sections, 20 span sections

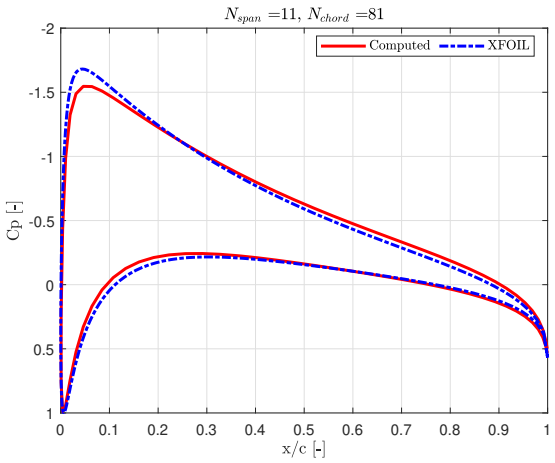

(g) 71 chord sections, 20 span sections

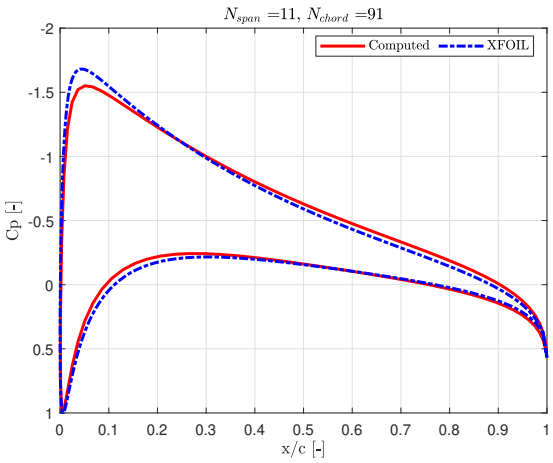

(h) 81 chord sections, 20 span sections

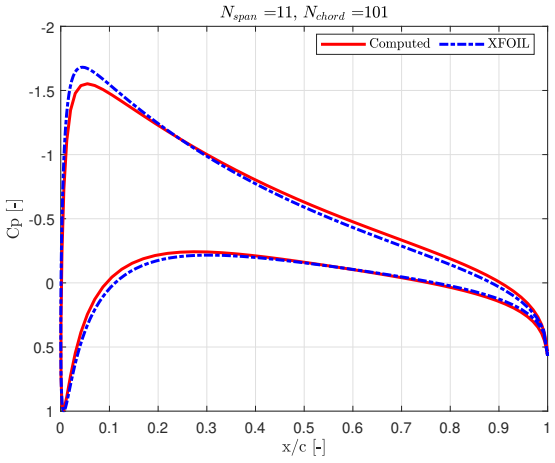

(i) 91 chord sections, 20 span sections

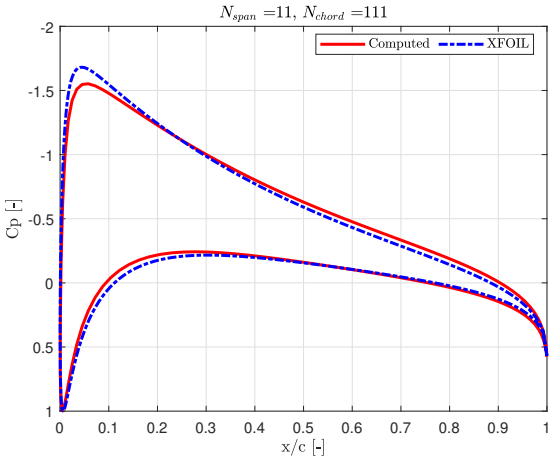

(j) 101 chord sections, 20 span sections

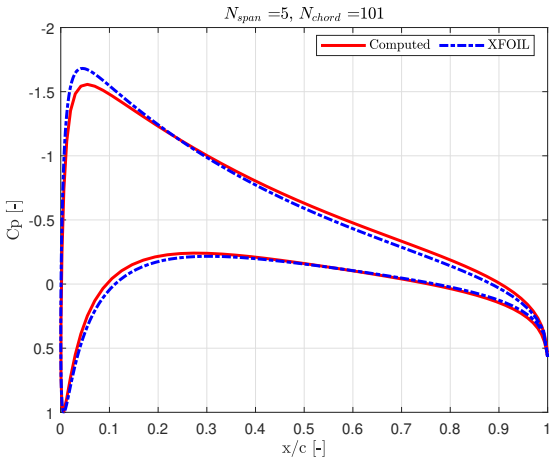

(k) 51 chord sections, 4 span sections

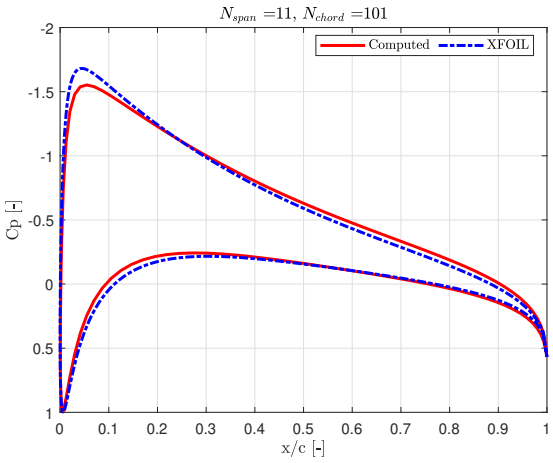

(l) 51 chord sections, 10 span sections

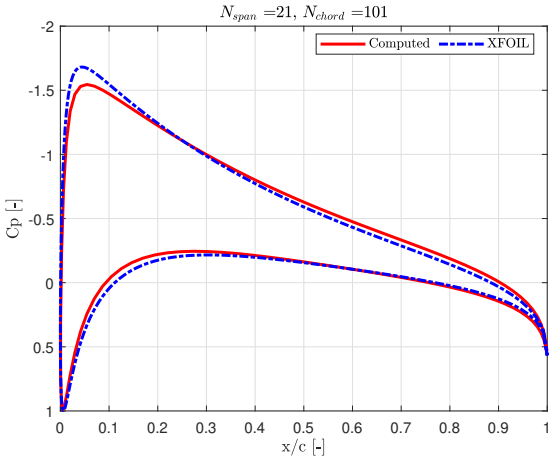

(m) 51 chord sections, 20 span sections

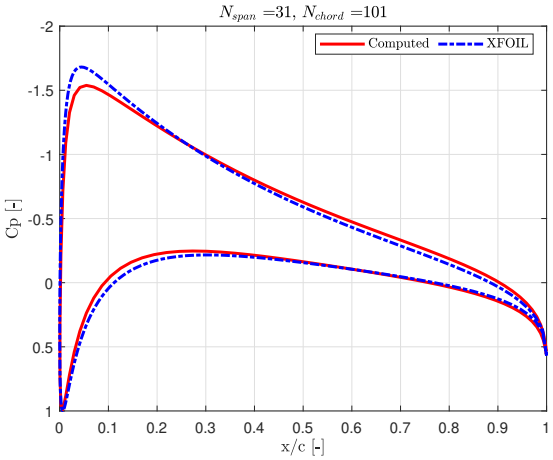

(n) 51 chord sections, 30 span sections

List of Figures

List of Tables